JACS
JOURNAL OF THE AMERICAN CHEMICAL SOCIETY
pubs.acs.org/JACS
Article

High-Throughput Screening and Automated Data-Driven Analysis of the Triplet Photophysical Properties of Structurally Diverse, Heteroleptic Iridium(III) Complexes

Stephen DiLuzio, Velabo Mdluli, Timothy U. Connell, Jacqueline Lewis, Victoria VanBenschoten, and Stefan Bernhard*

Cite This: J. Am. Chem. Soc. 2021, 143, 1179−1194
Read Online

ACCESS | Metrics & More | Article Recommendations | Supporting Information

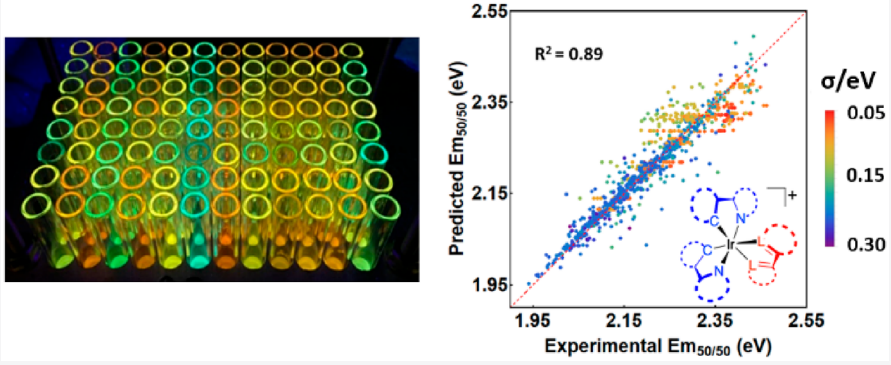

ABSTRACT: Steady state emission spectra and excited state lifetimes were measured for 1440 distinct heteroleptic $[Ir(C^N)_2(N^N)]^+$ complexes prepared via combinatorial parallelized synthesis; 72% of the complexes were found to be luminescent, and the emission maxima of the library spanned the visible spectrum (652−459 nm). Spectral profiles ranged from broad structureless bands to narrow emissions exhibiting vibrational substructure. Measured excited state lifetimes ranged between ∼0.1−14 μs. Automated emission spectral fitting with successive Gaussian functions revealed four distinct measured classes of excited states; in addition to well understood metal−ligand to ligand-charge transfer (^{3}MLLCT) and ligand-centered (^{3}LC) excited states, our classification also identified photophysical characteristics of less explored mixed ^{3}MLLCT/^{3}LC states. Electronic structure features obtained from DFT calculations performed on a large subset of these Ir(III) chromophores offered clear insights into the excited state properties and allowed the prediction of structure/luminescence relationships in this class of commonly used photocatalysts. Models with high prediction accuracy (R^2 = 0.89) for emission color were developed on the basis of experimental data. Furthermore, different degrees of nuclear reorganization in the excited state were shown to significantly impact emission energy and excited state lifetimes.

Downloaded via CARNEGIE MELLON UNIV on February 24, 2021 at 17:31:42 (UTC).
See https://pubs.acs.org/sharingguidelines for options on how to legitimately share published articles.

INTRODUCTION

Second and third row d^6 transition metals, specifically Ru(II), Re(I), Os(II), and Ir(III), form photoactive coordination complexes suitable for varied applications including light emitting diodes, oxygen sensing, organic photocatalysis, bioimaging, photodynamic therapy, and solar fuel generation.[1−27] Heteroleptic $[Ir(C^N)_2(N^N)]^+$ complexes (where C^N is a cyclometalating 2-phenylpyridyl ligand and N^N is a 1,2-diimine ancillary ligand, Figure 1A) are popular scaffolds due to their modular synthesis, enhanced photostability, and long-lived triplet excited state lifetimes arising from strong spin−orbital effects of Ir(III).[28−31] Large ligand-field splitting, caused by the high quantum number of the central Ir *d*-electrons and the strongly σ-donating carbanions of the cyclometalating ligands, significantly destabilizes metal-centered (MC) antibonding orbitals compared to other 4*d* and 5*d* metal ion complexes.[32] The substantial increase in these e_g*-like orbitals inhibits thermal population of the deactivating ^{3}MC excited state and allows the large variability in emission color of reported Ir(III) complexes, spanning the visible spectrum (Figure 1A).

The photophysical properties of $[Ir(C^N)_2(N^N)]^+$ complexes can be synthetically engineered by the judicious tuning of the highest occupied and lowest unoccupied molecular

Received: November 24, 2020
Published: January 7, 2021

© 2021 American Chemical Society

https://dx.doi.org/10.1021/jacs.0c12290
J. Am. Chem. Soc. 2021, 143, 1179−1194

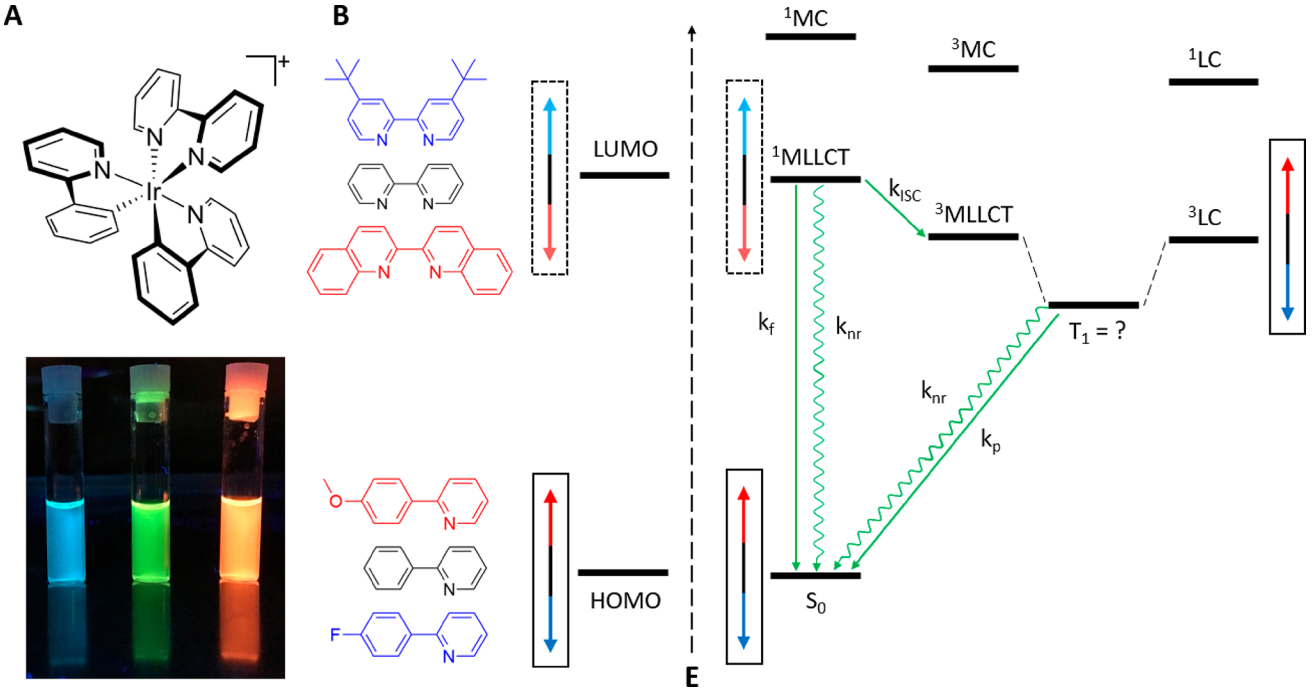

Figure 1. (A) Archetypal $[Ir(C^N)_2(N^N)]^+$ complex where cyclometalating and ancillary ligand are 2-phenylpyridine and 2,2′-bipyridine, respectively. Ligand manipulation affords Ir(III) complexes that emit across the visible spectrum. (B) Jablonski diagram of the pertinent transitions in Ir(III) photophysics. Precise ligand control allows independent tuning of the HOMO and LUMO energies. It is difficult to predict the interplay between the ^{3}MLLCT/^{3}LC states and subsequent identification of the lowest triplet excited state.

orbital (HOMO and LUMO, respectively) energies. For the vast majority of these complexes, the HOMO is predominantly localized over the Ir(III) *d* orbitals and π orbitals on the phenyl ring of the cyclometalating ligand, while the LUMO usually comprises π^* orbitals on the ancillary ligand. The lowest energy absorption in $[Ir(C^N)_2(N^N)]^+$ is therefore assigned to a $d\pi \rightarrow \pi^*$ metal/ligand-to-ligand charge transfer (MLLCT).[28] The ^{1}MLLCT transition is typically the dominant visible-wavelength transition ($\varepsilon \approx 1000-5000\ M^{-1}\ cm^{-1}$) which then undergoes rapid intersystem crossing to the ^{3}MLLCT excited state (Figure 1B).[33] The tuning of the gap between HOMO and LUMO orbitals is possible through the functional group modification of the cyclometalating or ancillary ligand, respectively; electron withdrawing groups stabilize while donating groups destabilize the corresponding orbital energy levels.[31] In this particular family of $[Ir(C^N)_2(N^N)]^+$ complexes, the triplet excited state can be influenced from strong exchange interactions that significantly stabilize the ^{3}LC state localized on the cyclometalating ligand (Figure 1B).[34] Depending on the relative energies of the ^{3}MLLCT and ^{3}LC states, internal conversion following the initial population of the ^{3}MLLCT may result in either a mixed ^{3}MLLCT/^{3}LC or an entirely ^{3}LC lowest lying excited state (T_1).[35−37] Despite the facile manipulation of emission wavelength afforded by altering the coordination environment, structural parameters that affect excited state lifetime and photochemical reactivity are not well understood.

Emission lifetime is often critical for the desired application of a newly prepared phosphor, for instance, short lifetimes prevent dye degradation in light emitting diodes while diffusion controlled bimolecular interactions necessary in organic photocatalysis benefit from longer-lived excited states. Generally, the emission spectral shape from a pure ^{3}MLLCT excited state is broad and featureless with a lifetime <2 μs, while emission from a pure ^{3}LC state exhibits vibronically resolved peaks and relatively longer lifetimes due to the decreased metal character of the excited state.[37−41] Unfortunately, prediction of a novel $[Ir(C^N)_2(N^N)]^+$ complex triplet configuration, an integral part of stability and reactivity, is often challenging as the π^* orbitals of the cyclometalating and ancillary ligand are sensitive to the environment and often close in energy.[42] For instance, solvatochromic effects can cause stabilization and emission from the ^{3}MLLCT in polar solvents while ^{3}LC emission can be observed for the same compound in the solid state or less polar solvents.[33,42] Experimental efforts to characterize triplet excited state processes require highly specialized and expensive ultrafast spectroscopy while theoretical approaches, such as time-dependent density functional theory (TD-DFT), are not only time-consuming and computationally intensive but also have trouble modeling triplet transitions accurately.

Despite the considerable ligand diversity in reported Ir(III) complexes, a lack of standardized analytical procedures (e.g., spectrometer response, concentration, solvent) prevents the ready comparison of literature values or the creation of large databases to support quantum chemical or machine learning-based prediction efforts. We have previously demonstrated the effectiveness of combinatorial synthesis to generate novel heteroleptic Ir(III) phosphors.[10,43] Here, we combine this approach with high-throughput, parallel synthesis techniques to measure the steady-state emission spectra and excited-state lifetime of an unprecedented library of 1440 structurally diverse complexes. Automated analysis of the experimental emission spectra and lifetime provides a framework for assigning the nature of the triplet excited state. DFT calculations were used to understand the effects of a complex's electronic structure on its photophysical properties. The subsequent correlation of ligand environment and photo-

https://dx.doi.org/10.1021/jacs.0c12290
J. Am. Chem. Soc. 2021, 143, 1179−1194

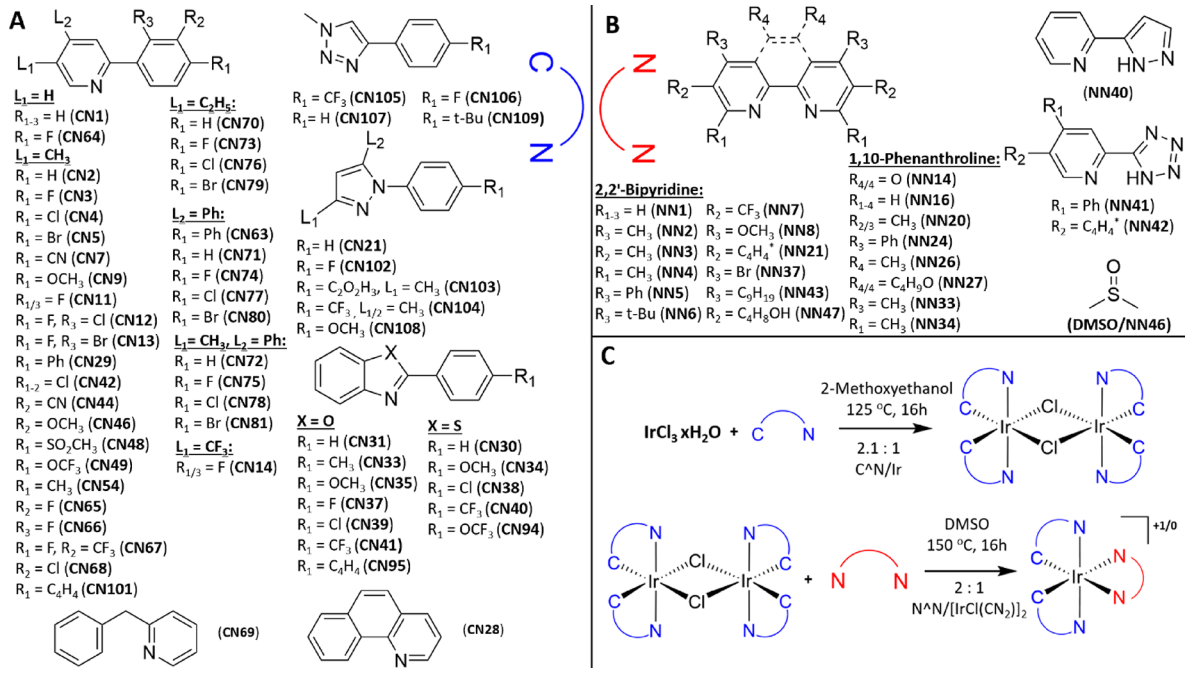

Figure 2. Scope of the combinatorial library. (A) Cyclometalating (C^N) and (B) ancillary (N^N) ligands used in library construction. Ligands are labeled using descriptors of a larger ligand library employed in our laboratory. (C) Precursor $[Ir(Cl)(C^N)_2]_2$ dimers were prepared via batch before high-throughput parallel synthesis of $[Ir(C^N)_2(N^N)]^+$ complexes. DMSO is labeled **NN46** to maintain consistency across the set and facilitate computational efforts in this work. All ligand structures are shown in the Supporting Information (Tables S1, S2).

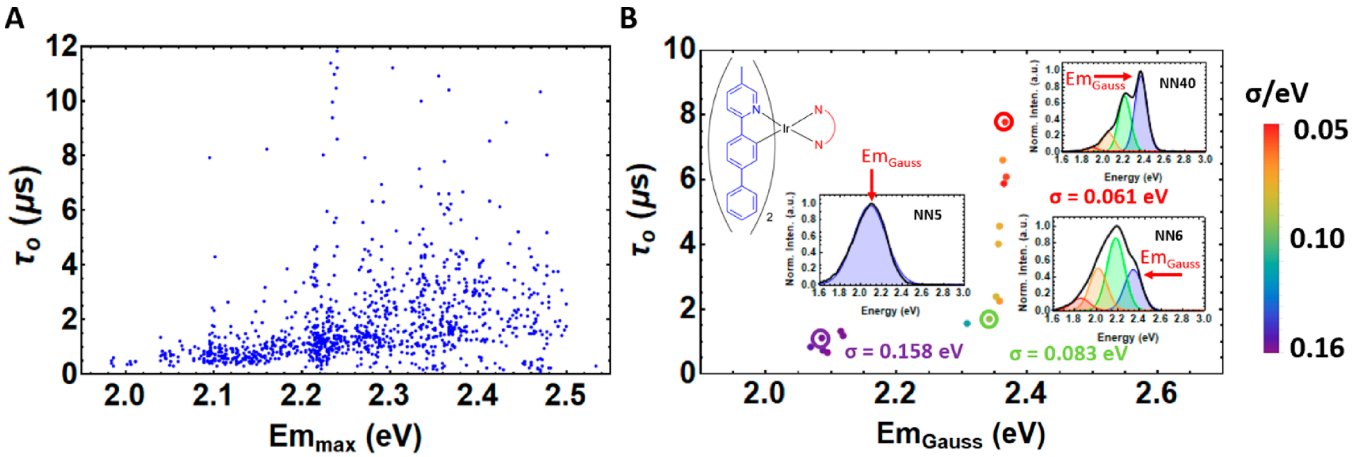

Figure 3. (A) Emission peak maxima (Em_{max}) vs lifetime (τ_0) of all emissive Ir(III) complexes. 72% of the library composed of 1140 possible species formed emissive complexes. (B) Em_{Gauss} vs τ_0 for $[Ir(\mathbf{CN29})_2(N^N)]^+$ (**CN29:** 2-(1,1′-biphenyl]-4-yl)-5-methylpyridine) complexes with overlaid Gaussian functions for the ancillary ligands **NN1-NN8, NN16, NN20-NN21, NN26-NN27, NN33-NN34, NN40-NN43, NN47.** Standard deviation, or width in eV, of the optimally fitted Gaussian function(s) (σ) corresponds to plot point color. The same color code for σ is used throughout this paper.

physics highlights several structural characteristics that influence the photophysical properties, such as the degree of ^{3}LC/^{3}MLLCT mixing or the extent of nuclear reorganization, upon excitation or relaxation. The finding of these trends represents an important development toward computational prediction and synthetic control of the photophysical properties in these widely used luminescent transition metal complexes.

RESULTS AND DISCUSSIONS

We prepared a structurally diverse library of Ir(III) complexes using 60 cyclometalating and 24 ancillary ligands, totaling 1440 distinct possible species. Cyclometalating ligands included derivatives of the archetypal 2-phenylpyridine, 1-phenylpyrazole, 1-methyl-4-phenyl-1*H*-1,2,3-triazole, 2-phenylbenzoxazole, and 2-phenylbenzothiazole, as well as benzo[*h*]-quinoline and 2-benzylpyridine (Figure 2A). Ancillary ligands belonged to one of four classes: highly diverse derivatives of 2,2′-bipryidine and 1,10-phenanthroline as well as select tetrazoles and pyrazoles that deprotonate on metal coordination (Figure 2B). Dimethyl sulfoxide (**NN46**) was also used to form the baseline *solvato* complexes $[Ir(C^N)_2(DMSO)(Cl)]^+$. Precursor Ir(III) dimers were prepared in batch before parallel synthesis of the 1440 distinct $[Ir(C^N)_2(N^N)]^+$ complexes (Figure 3C). Emission spectra and lifetimes were measured under anaerobic conditions. The success of the

https://dx.doi.org/10.1021/jacs.0c12290
J. Am. Chem. Soc. 2021, 143, 1179−1194

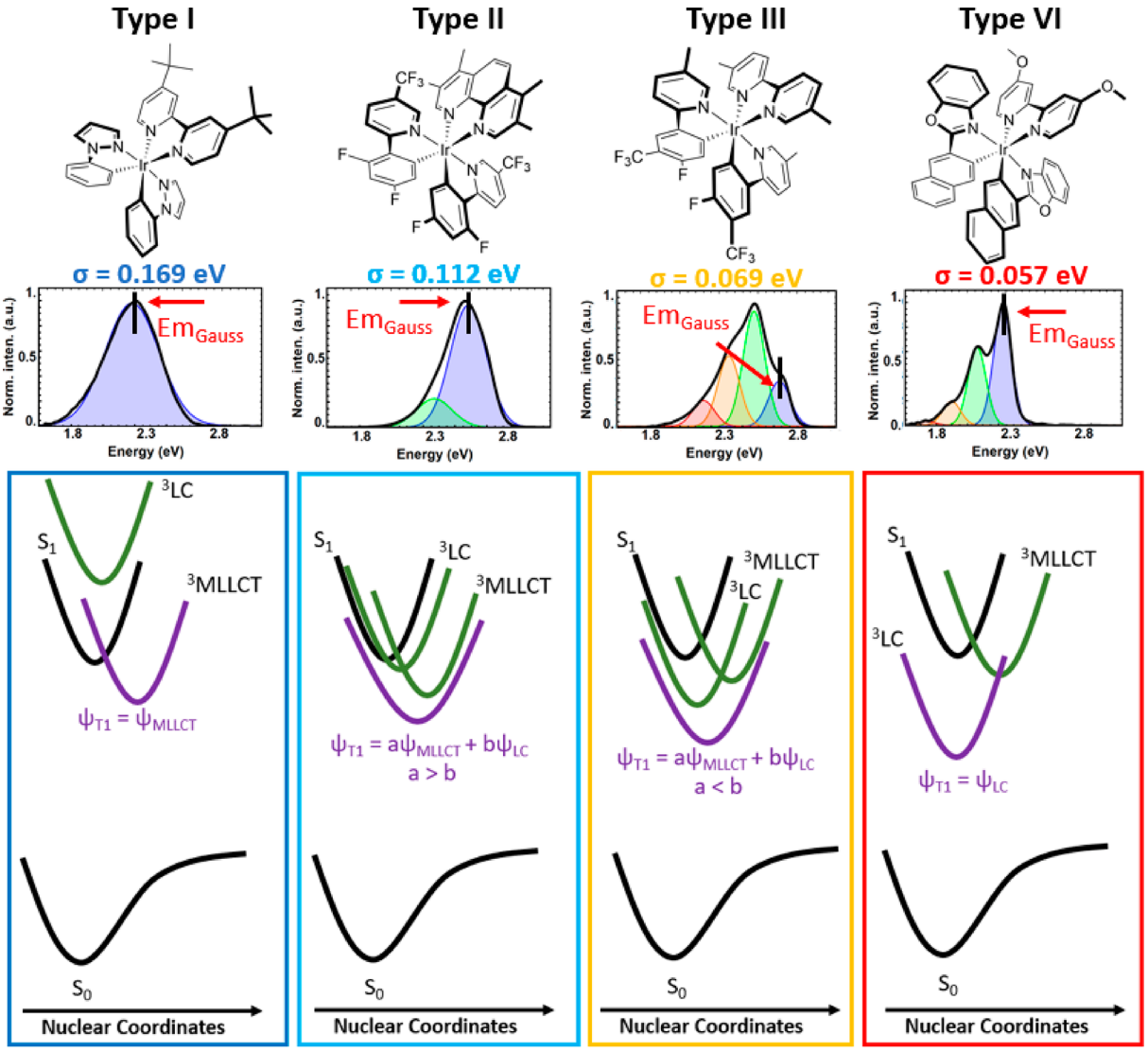

Figure 4. Representative Ir(III) complexes of each excited state (Types I–IV) and the corresponding excited state energy diagrams. The emission spectra and Gaussian function fitting parameters are strongly dependent on the electronic structure characteristics of T_1 such as the energy alignment and mixing predisposition of the pure ^{3}MLLCT and ^{3}LC states. The increasing vibronic substructure of the spectra reflects the coupling of the ^{3}LC state to the C^N ligands ring breathing modes commonly observed in $\pi \rightarrow \pi^*$ transitions. Similar nuclear geometries of the excited state and ground state leads to more pronounced 0–0 transition. The color coding refers to the σ scaling bar in Figure 3.

combinatorial synthesis was monitored using ^{19}F NMR spectroscopy of complexes with fluorinated cyclometalating or ancillary ligands. Formation of the desired heteroleptic $[Ir(C^N)_2(N^N)]^+$ product was observed in high conversions, albeit for a small number of ancillary ligands with steric hindrances adjacent to the chelating nitrogen binding was inhibited (**NN4**, **NN21**, and **NN37**) with these reaction conditions (Figures S1–S8). Heteroleptic complexes formed from precursor dimers containing **CN37** and **CN39** exhibited dual exponential decay in their excited state lifetime; however, the high-throughput synthesis resulted in a mixture of the *solvato* and heteroleptic complex (Figure S9). The additional emission likely occurs from the *solvato* complex as a result of the extended π system of these particular C^N ligands. Representative complexes prepared using traditional methods showed identical spectral shape with their high-throughput screening counterparts (Figure S10), indicating that all emissive compounds with a single exponential decay in excited state lifetime represent the formation of the expected heteroleptic $[Ir(C^N)_2(N^N)]^+$ complex.

Excited State Classification. Emission peak maxima (Em_{max}) ranged from ~1.9–2.5 eV, while luminescence lifetimes spanned 2 orders of magnitude, between ~0.1–12 μs (Figure 3A).

Luminescent lifetimes were accurately fitted using a single exponential decay. Finding single exponential decay patterns indicates that no emissive byproducts were formed during the parallel synthetic procedure. We expected that comparing the emission spectra and lifetime of the emissive compounds would provide insight into the inner workings of the excited state dynamics as it may better capture the large difference in electronic configuration of the ^{1}MLLCT and the lowest lying triplet excited state. Despite a rough correlation between increasing Em_{max} and lifetime, the spread of experimental data complicated our initial attempts to extract meaningful information from the synthesized library (Figure 3A). To aid in explaining this large experimental data set, feature extraction

https://dx.doi.org/10.1021/jacs.0c12290
J. Am. Chem. Soc. 2021, 143, 1179–1194

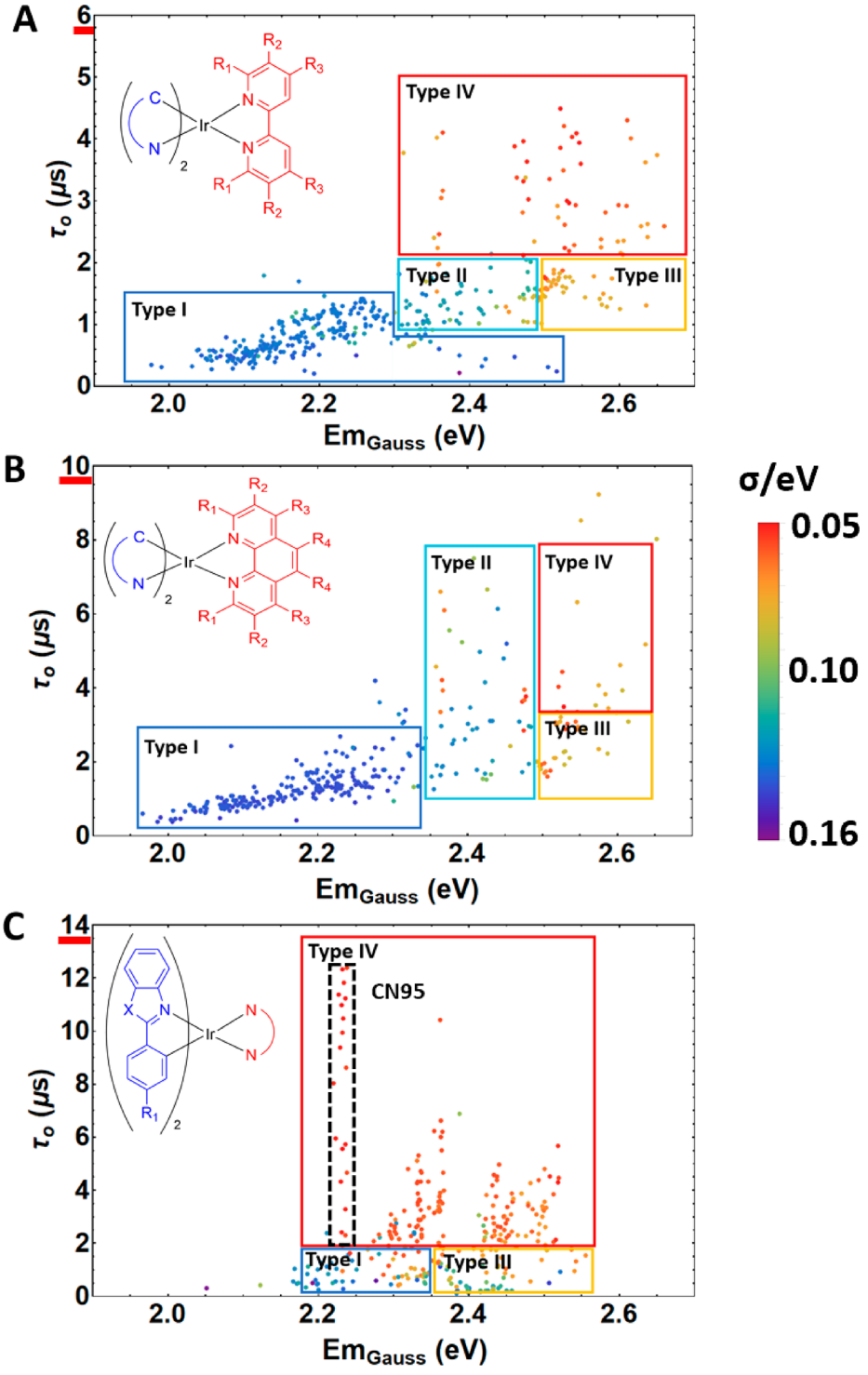

Figure 5. Subdivision of Em_{Gauss} vs τ_o graphs into three sets of structurally similar Ir(III) complexes. Standard deviation of fitted Gaussian function(s) (σ) corresponds to plot point color: (A) 2,2′-bipyridine ancillary ligands **NN1-NN3, NN5-NN6, NN8, NN40, NN43, NN47** with **CN1-CN5, CN7, CN11-CN13, CN29, CN42, CN46, CN48-CN49, CN54, CN70-CN81, CN64-CN67, CN101-CN109**; (B) 1,10-phenanthroline ancillary ligands **NN16, NN20, NN24, NN26, NN27, NN33-NN34** with the same set of C^N ligands used for part A; (C) 2-phenylbenzoxazole and 2-phenylbenzothiazole (X = O, S) derivatives **CN30-CN41, CN94-CN95** (dashed box, **CN95**) with all N^N ligands. Both parts A and B do not contain 2-phenylbenzoxazole and 2-phenylbenzothiazole C^N ligands. Note the change in magnitude of the *y*-axis.

from emission spectra was carried out by applying successive fitting of the spectral profile using one to four Gaussian functions. Em_{max} is now replaced with Em_{Gauss}, which is characterized by the highest energy peak of the fitted Gaussian function(s). For ^{3}MLLCT emission, Em_{Gauss} does not significantly deviate from Em_{max}; however, Em_{Gauss} for ^{3}LC states represents the Em_{0-0} vibronic transition and may differ from the Em_{max}. Fits comprising more than two Gaussian functions were forced to be equally spaced and of the same standard deviation (σ), or width, reflecting the vibronic substructure observed in some of these chromophores. It is important to note that addition of more Gaussian functions for

https://dx.doi.org/10.1021/jacs.0c12290
J. Am. Chem. Soc. 2021, 143, 1179−1194

fitting necessarily reduces the fit's standard deviation. Visualizing this fitted width on a plot of Em_{Gauss} vs excited state lifetime (τ_o) for the single class of Ir(III) complexes $[Ir(\mathbf{CN29})_2(N^N)]^+$, revealed two different behavioral trends (Figure 3B). At low energies (~2.1 eV), emission was characteristic of ^{3}MLLCT with structureless spectral profile, lifetimes ~1 μs and a good fit using a single broad Gaussian function. Complexes with emission maxima greater than 2.3 eV instead required four Gaussian functions to achieve an adequate fit, indicating a transition to the ^{3}LC excited state. Complexes that exhibit such structured emission also exhibit minimal deviation from a common Em_{Gauss} (±0.02 eV), indicating an excited state emission energy predominantly dictated by the $^3\pi^*_{(C^N)} \rightarrow d\pi_{(C^N)}$ transition energy with minor influence from the ancillary N^N ligand.

Extrapolating this approach to all emission spectra revealed four distinct types of excited states, characterized by the Gaussian function fitting parameters, for $[Ir(C^N)_2(N^N)]^+$ complexes across the entire tested library: Type I, exclusively ^{3}MLLCT; Type II, mixed ^{3}LC/^{3}MLLCT with mostly ^{3}MLLCT character; Type III, ^{3}LC dominated excited states with some ^{3}MLLCT character; and pure ^{3}LC states (Type IV). While the geometry of the ^{3}LC state is similar to the ground state nuclear arrangement, interaction with ^{3}MLLCT state (Type III) seemingly causes a more substantial geometry change compared to Type IV complexes (Figure 4). Complexes that exhibit Type I excited states are characterized by electron rich cyclometalating ligands or an electron deficient ancillary ligand, resulting in a pure ^{3}MLLCT triplet state (T_1). Increasing the energy gap, through the introduction of electron withdrawing substituents on the cyclometalating ligand or electron donating substituents on the ancillary ligand, will consequently reduce the energy difference between the ^{3}MLLCT and ^{3}LC energy levels. Mixing occurs once these two states are sufficiently close in energy, resulting in a T_1 state denoted as Type II. These complexes are characterized by the asymmetric shape of the emission spectra and a single exponential decay in exited state lifetime, indicative of emission from a single T_1 state. Continued HOMO stabilization and/or LUMO destabilization eventually results in complexes with Type III/IV excited states revealing increasing amounts of ^{3}LC character. Type III complexes are characterized by a vibrational substructure that indicates differing geometries of the singlet ground and triplet excited state, resulting in a nondominant $Em_{0-0}(Em_{Gauss})$ vibronic emission peak (Figure 4) and often contain higher energy π^* orbitals on the cyclometalating ligand compared to Type IV complexes. A further decrease in the π^* orbital energy of the cyclometalating ligand results in Type IV excited states where larger Em_{0-0}/Em_{0-1} vibronic peak ratios (≥1) indicates similar T_1/S_0 geometries. Conceptually, the shift from Type I to Type III/IV excited states represents intramolecular electron transfer from the ancillary ligand to a cyclometalating ligand following the initial ^{1}MLLCT excitation.

We next applied this excited state classification to larger families of structurally diverse Ir(III) complexes. Emissive complexes containing 2-phenypyridine, 1-methyl-4-phenyl-1*H*-1,2,3-triazole, and 1-phenylpyrazole cyclometalating ligands and all 2,2′-bipyridine and pyrazole ancillary ligands reveal that the lifetimes of Type I excited states increase with increasing energy up to ~2.35 eV (Figure 5A). This emission energy represents a critical junction with respect to excited state morphology. Most complexes begin to exhibit an asymmetric spectral shape that requires two Gaussian functions for adequate fitting, and consequently, a decrease in the function's standard deviation. These properties, along with a lack of apparent vibronic substructure, are indicative of Type II complexes and continue to demonstrate a synchronous increase in emission maxima and lifetime. Only a small subset of complexes continued to exhibit ^{3}MLLCT Type I excited states >2.35 eV that decreased in lifetime with continued hypsochromic shift in emission (Figure 5A). All such complexes contained electron withdrawing and π^* destabilized cyclometalating ligands (derivatives of 1-methyl-4-phenyl-1H-1,2,3-triazole or 1-phenylpyrazole) paired with highly electron rich ancillary ligands; specifically the deprotonated pyrazole **NN40**, the most electron rich ancillary ligand studied. This combination of ligands represents the energetic limits of pure ^{3}MLLCT excited states; unable to access their highly destabilized ^{3}LC orbitals, population of the nonemissive ^{3}MC states followed by rapid nonradiative decay, explaining the decreasing excited state lifetimes with an increasingly blue-shifted emission. For the remaining complexes, as Em_{Gauss} reaches ~2.45 eV, spectra begin to reveal vibronic structure, indicating the transition to Type III/IV complexes and the continued decrease in the standard deviation of the fitted Gaussian functions (Figure 5A). These complexes also exhibit much greater variability in emission lifetime >2 μs consistent with a switch to ^{3}LC dominated excited states that exhibit a decreased participation of the deactivating metal centered state observed in ^{3}MLLCT excited states. While most of these complexes are high energy emitters (Em_{Gauss} > 2.5 eV), complexes involving cyclometalating ligands with large conjugated systems do demonstrate Type IV states at lower energies, such as the phenyl-substituted **CN29** (Figure 3B) and **CN63**.

Substitution of 2,2′-bipyridine derivatives with 1,10-phenanthroline reveals the same general trends; however, complexes with Type I excited states generally display longer, less varied ^{3}MLLCT lifetimes at any given emission energy (Figure 5B). Furthermore, only the most electron deficient cyclometalating ligands activate ^{3}LC states, and 1,10-phenanthroline containing complexes with Type III/IV excited states consequently appear at higher energy than their 2,2′-bipyridine analogues. We attribute these observations to an enhanced stabilization of π^* orbitals afforded by greater conjugation in 1,10-phenanthrolines. This same stabilization reduces the likelihood of populating ^{3}MC states, and no decrease in excited state lifetime was observed in complexes with emission maxima >2.3 eV.

Cyclometalating ligands with extended conjugation that stabilize the π^* orbitals, such as derivatives 2-phenylbenzoxazole and 2-phenylbenzothiazole, typically exhibit vibronic substructure and long lifetimes (Figure 5C). These complexes most often show Type III and Type IV excited states arising from the inherent π^*stabilization caused by the significant cyclometalating ligand conjugation. Em_{Gauss} appears independent of ancillary ligand, as exemplified by complexes containing **CN95** (Figure 5C, dashed box) that all emit at 2.23 eV ± 0.01 eV. Overall, the subset depicted in Figure 5C exhibits a narrower spread of Em_{Gauss} (2.1−2.6 eV) compared to the full library (1.9−2.7 eV), which we attribute to the inhibition of independent orbital energy tuning, a result of the prominent population of ^{3}LC states on the cyclometalating ligand. Generally, the standard deviation of fitted Gaussian

https://dx.doi.org/10.1021/jacs.0c12290
J. Am. Chem. Soc. 2021, 143, 1179−1194

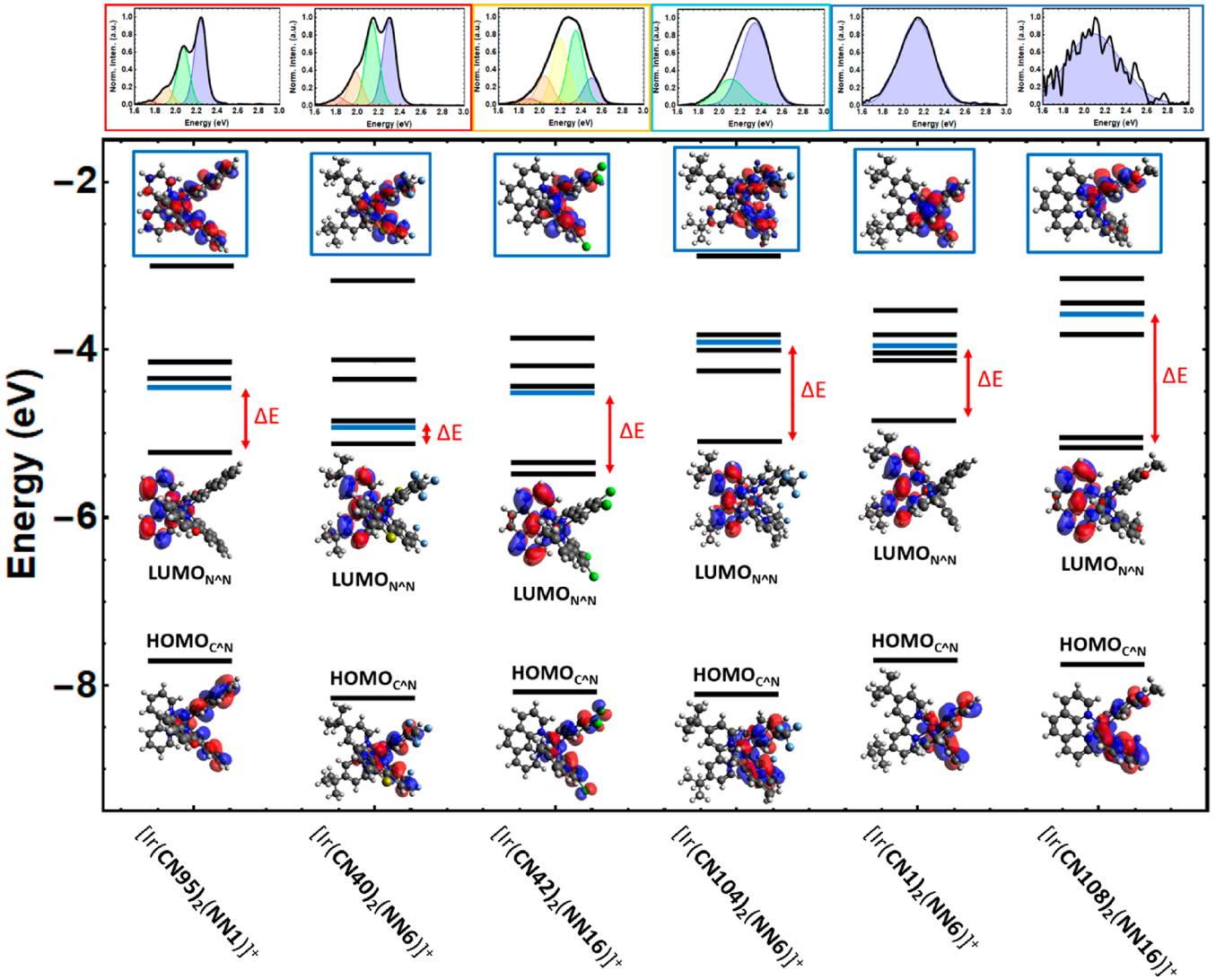

Figure 6. DFT calculated orbital energy level diagrams of the singlet ground state for six representative $[Ir(C^N)_2(N^N)]^+$ complexes that span Types I–IV excited states. Fitted emission spectra, orbital composition distributions, and pertinent orbital labels are included. The first unoccupied π^* orbital located on the C^N ligand is marked in blue. The energy difference between this orbital and the LUMO (ΔE) was used as a tool to find excited state trends (Figure 7A).

functions decreased as excited state lifetime increased and is therefore a good measure of the degree of ligand centered character in the T_1 state. It was also observed that there is a consistent bathochromic shift in emission (~0.2 eV) between related complexes containing 2-phenylbenzothiazole and 2-phenylbenzoxazoles, assigned to greater stabilization of π^* orbital energy levels of the ^{3}LC excited state from the sulfur atom compared to those of the more electronegative oxygen atom.

Density Functional Theory Modeling. We used density functional theory (DFT) to calculate the singlet ground state of 306 randomly selected complexes, containing a mixture of Types I–IV excited states, to determine the relationship between π^* orbitals of the cyclometalating and ancillary ligands. Computational analysis confirmed that HOMO orbitals were predominately localized on the Ir(III) center and phenyl rings of the cyclometalating ligand, while the LUMO resided on the ancillary ligand (Figure 6). Our unprecedently large DFT library confirmed previously observed trends across much smaller families of Ir(III) complexes.[37−44] The calculated singlet ground state orbitals are not an adequate representation of the triplet excited state measured experimentally, failing to account for nuclear reorganization and exchange interactions. Despite this, we observed a correlation between the energy difference of the lowest lying π^* orbitals located on the ancillary (LUMO) and on the cyclometalating ligands, depicted as ΔE (Figure 6), and the standard deviation (σ) of the Gaussian function in fitted emission spectra (Figure 7A). This mutual increase signifies the successive change in excited state composition, with mixed Type II/III excited states residing between the Type IV (^{3}LC) and Type I (^{3}MLLCT) extremes. As the singlet π^* orbitals of each ligand become closer in energy, it is increasingly likely that the lowest lying triplet state, responsible for emission, will be of ^{3}LC character. This implies that intramolecular electron transfer from the initially populated ancillary to the cyclometalating ligand is thermodynamically favorable after conversion to the triplet state. This switch is facilitated by the large singlet−triplet stabilization energy traditionally observed in these $\pi \rightarrow \pi^*$ like transitions.[34] We also performed

https://dx.doi.org/10.1021/jacs.0c12290
J. Am. Chem. Soc. 2021, 143, 1179−1194

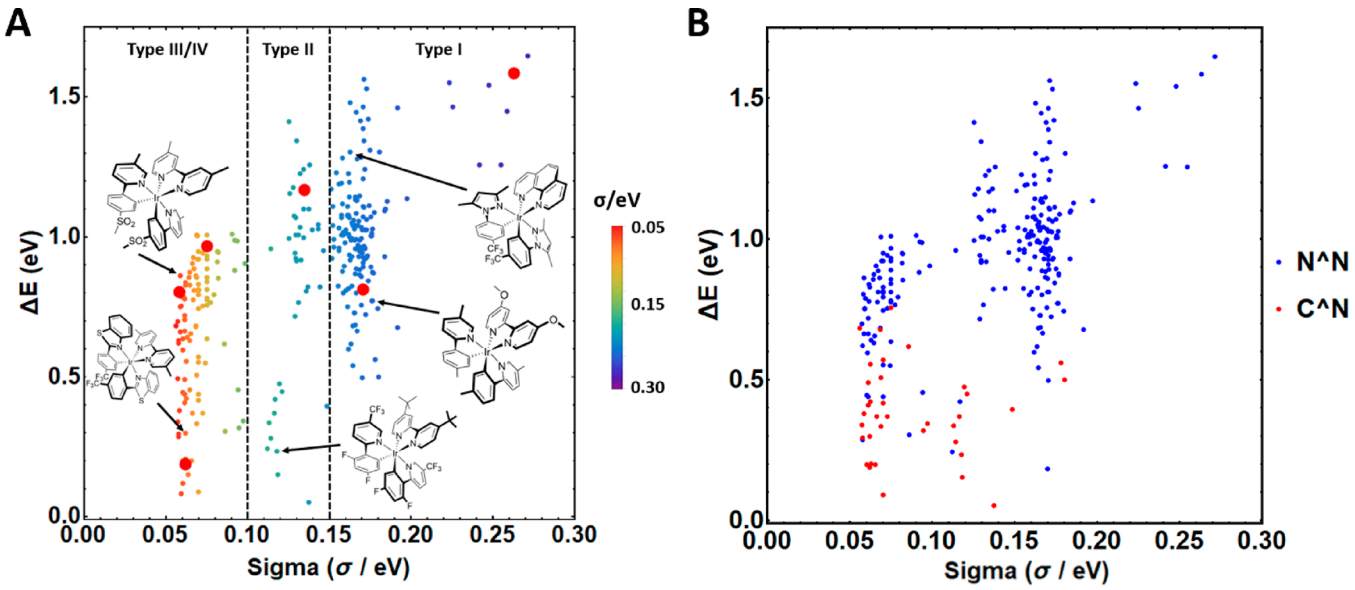

Figure 7. Energy difference of ancillary and cyclometalating ligand π^* orbitals (ΔE) vs σ for the 306 complexes with computationally calculated energy levels (A). Complexes included in Figure 6 correspond to the highlighted red data points in part A. Dependence of the location of the HSOMO controlled by ΔE and σ (B).

triplet DFT based calculations on the same complexes to probe the location of the HSOMO, which showed good agreement between Type IV ($\sigma < 0.10$) and Type I ($\sigma > 0.15$) excited state morphologies (Figure 7B). Some triplet calculations of complexes with Type II excited states showed the HSOMO distributed across the entire complex (Figure S11). A few complexes, for instance, the widely used $[Ir(\mathbf{CN1})_2(\mathbf{NN6})]^+$, included in this computational analysis exhibited a spectral shape and fitting parameters indicative of a Type I excited state but π^* orbital energy differences (ΔE) more suggestive of Type III/IV states (Figure 7A), indicating that other factors control the morphology of the triplet excited state. Furthermore, numerous Type II compounds have ΔE values indicative of an ^{3}LC, Type IV state configuration. These occurrences likely arise from differences between the singlet DFT geometry and that of the relaxed T_1 state, where internal conversion likely alters the energy of the HSOMO.

Satisfied with our ability to understand the factors controlling the electronic configuration of the lowest lying triplet state, we considered what the ligand structure might reveal about Em_{Gauss} and spectral shape as well as emission lifetime. The precise control of photophysical properties, through rational design of ligand structure, is particularly advantageous across the many research fields where heteroleptic $[Ir(C^N)_2(N^N)]^+$ are employed. The next two sections center on control and prediction of excited state lifetime and emission energy.

Factors Affecting Excited State Lifetime. Differences in excited state lifetime in heteroleptic $[Ir(C^N)_2(N^N)]^+$ complexes typically result from vibrational deactivation described by the Energy Gap Law, ease of thermal population of the ^{3}MC state, and the contribution of Ir *d* orbitals in the excited state, the latter of which is responsible for the increased lifetime in ^{3}LC states.[31] One less explored avenue for deactivation is the change in nuclear configuration of the excited state relative to the ground state after Franck−Condon excitation.

Out of all the successfully synthesized complexes, as determined from ^{19}F NMR spectroscopy, 86% formed highly emissive excited states with lifetimes ≥100 ns. Nonemissive or weakly emissive complexes were typically formed with the electron deficient ligands **NN7** or **NN14**, despite confirmation of the formed $[Ir(C^N)_2(N^N)]^+$ heteroleptic product via ^{19}F NMR spectroscopy (Figures S1, S2, S4, S5, S7, S8). Figure 5A,B shows an increase in excited state lifetime as Em_{Gauss} increases, thus the lack of emission from complexes containing the above ancillary ligands are rationalized through Energy Gap Law arguments where k_{nr} is too large to observe an emissive excited state due to detrimental LUMO stabilization. **CN46** is the only C^N ligand in this set that almost exclusively forms nonemissive complexes, which has been previously reported for some ancillary ligands.[45]

Energy Gap Law behavior is only observed in Type I excited states (Figure 5A,B), highlighting the importance of the spin−orbit coupling effects of iridium. Although higher rates of intersystem crossing promote population of the triplet excited state after singlet excitation, it will also promote higher rates of intersystem crossing for deactivation, resulting in faster depletion of the excited state. Spin density values of Ir in the triplet state are readily obtained through triplet DFT calculations and describe the contribution of Ir in the triplet excited state.[46] Indeed ^{3}MLLCT (Type I) complexes exhibit larger Ir spin density values on average (∼0.5)(Figure S12) than the corresponding Type II−Type IV, ^{3}LC counterparts (∼0.1−0.45). No direct correlations can be drawn between the spin density values of Ir and lifetime within the same excited state electronic configuration; however, ^{3}LC excited states show substantially more deviation of lifetime.

The remaining two factors controlling excited state lifetimes are population of the quickly deactivating and nonradiative ^{3}MC state and differing degrees of nuclear reorganization in the excited state, which may depend on ligand morphology. Rates of nonradiative decay in heteroleptic $[Ir(C^N)_2(N^N)]^+$ complexes will depend on both the inherent vibrational wave function overlap between S_0 and T_1, as dictated by the Energy

https://dx.doi.org/10.1021/jacs.0c12290
J. Am. Chem. Soc. 2021, 143, 1179−1194

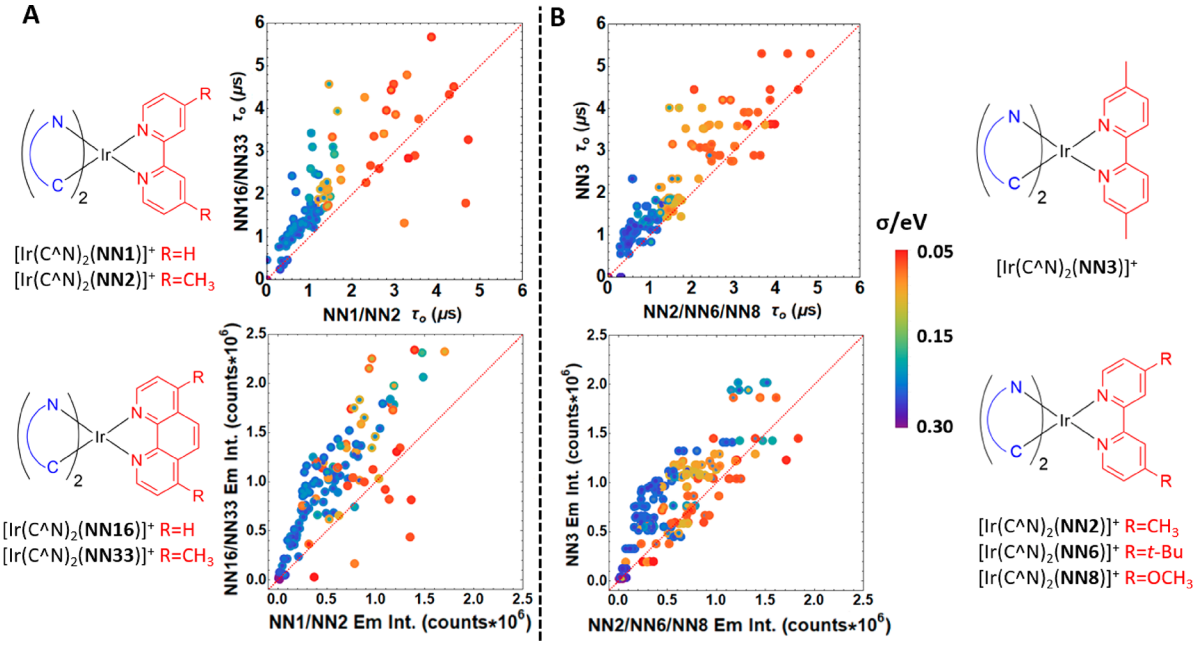

Figure 8. Effect of ancillary ligand morphology and substituent position on excited state lifetime (τ_o) and the emission spectra integral (Em Int.). Represented N^N ligands of the Ir(III) complexes discussed are shown. Overlaid comparison plots of τ_o and emission intensity (Em Int.) for complexes containing all C^N ligands with **NN16** vs **NN1** and the methyl substituted **NN33** vs **NN2** (A) and **NN2**/**NN6**/**NN8** vs **NN3** (B). Equivalent lifetimes or emission intensities will fall on y = x (red dashed line). Standard deviation of fitted Gaussian function(s) (σ) corresponds to plot point color; for each plot point, the outer ring corresponds to spectral fits of **NN16**/**NN33** (A) and of **NN3** (B) complexes, while the inner circle corresponds to those of **NN1**/**NN2** (A) and of **NN2**/**NN6**/**NN8** (B) complexes.

Gap Law, and the population of ^{3}MC states. Population of the ^{3}MC state is a temperature dependent process and involves an activation energy between interacting T_1 and ^{3}MC states.[47−50] In Figure 5A, an apparent decrease in excited state lifetime is observed in the Type I complexes as emission energy increases. As stated above, these complexes are derivates of the 1-phenylpyrazole and 1-methyl-4-phenyl-1H-1,2,3-triazole C^N ligands, where the increased π^* orbital energy levels on these ligands inhibit ^{3}LC state population in the complex. Thus, when the most electron rich N^N ligand is employed, **NN40**, more facile thermal population of the ^{3}MC states occurs, resulting in decreased lifetimes. Interestingly, antibonding orbitals containing significant metal contribution obtained from singlet ground state DFT calculations show their energies are much higher than the LUMO (~2 eV), rendering thermal population of a ^{3}MC state without geometry change unlikely. Recent work by Wang et al. showed that MC states are readily perturbed through change of the coordination environment, specifically elongation of the Ir−N_{C^N} bond or via torsional bond rotation between the pyridyl moieties of the N^N ligand.[51] Significant nuclear distortion of the N^N ligand has been proposed as a mode of vibronic relaxation after Franck−Condon excitation in this class of Ir complexes.[52] This distortion, which weakens coordination bond strength, occurs through torsional bond rotation, lowering the ^{3}MC state energy and allowing thermal population. An analogous effect has been observed with Ru(II) chromophores, where weakened ligand coordination strength promotes ^{3}MC population.[53,54]

Probing nuclear reorganization pathways in an excited state is a challenging task and is not feasible on the scale of this data set; however, the effect of ancillary ligand torsional bond on the ^{3}MC states should result in distinct photophysical properties of structurally different classes of compounds, namely, 2,2′-bipyridine compared to the structurally rigid 1,10-phenanthroline. Lifetime comparisons between complexes containing 1,10-phenanthroline (**NN16**) and 2,2′-bipyridine (**NN1**) as well as 4,7-dimethyl-1,10-phenanthroline (**NN33**) and 4,4′-dimethyl-2,2′-bipyridine (**NN2**) with the same C^N ligand show that the structural rigidity of the 1,10-phenanthroline backbone overwhelmingly yields longer lifetimes especially in Type I complexes but also frequently in Type II−Type IV complexes (Figure 8A). Furthermore, **NN16** and **NN24** complexes depict much brighter emission intensities compared to those of **NN1** and **NN2**, suggesting suppressed population of nonradiative ^{3}MC states arising from increased structural rigidity. Figure 5A,B shows that Type I compounds with 2,2′-bipyridine (**5A**) or 1,10-phenanthroline (**5B**) based N^N ligands increase in excited state lifetimes as Em_{Gauss} increases, consistent with the Energy Gap Law; however, 1,10-phenanthroline based complexes exhibit on average excited state lifetimes that are 0.36 μs longer for the same Em_{Gauss} (Figure S13). This increase in lifetime for 1,10-phenanthroline based complexes relative to 2,2′-bipyridine can therefore not be rationalized through Energy Gap Law arguments. Treatment of the total k_{nr} as the summation of two nonradiative deactivation processes (eq 1)

$$k_{nr} = k_{nr}(E_{gap}) + k_{nr}(^3\text{MC}) \quad (1)$$

where $k_{nr}(E_{gap})$ is associated with inherent vibronic overlap between S_0 and T_1, and $k_{nr}(^3$MC) is associated with population of the nonradiative ^{3}MC state, rationalizes this observation. Inhibition of torsional bond rotation as a mode of vibronic relaxation results in larger activation energies for thermal population rates of the ^{3}MC state from the relaxed T_1 configuration due to the stronger coordination strength of phenanthroline-based ancillary ligands in the excited state.

https://dx.doi.org/10.1021/jacs.0c12290
J. Am. Chem. Soc. 2021, 143, 1179−1194

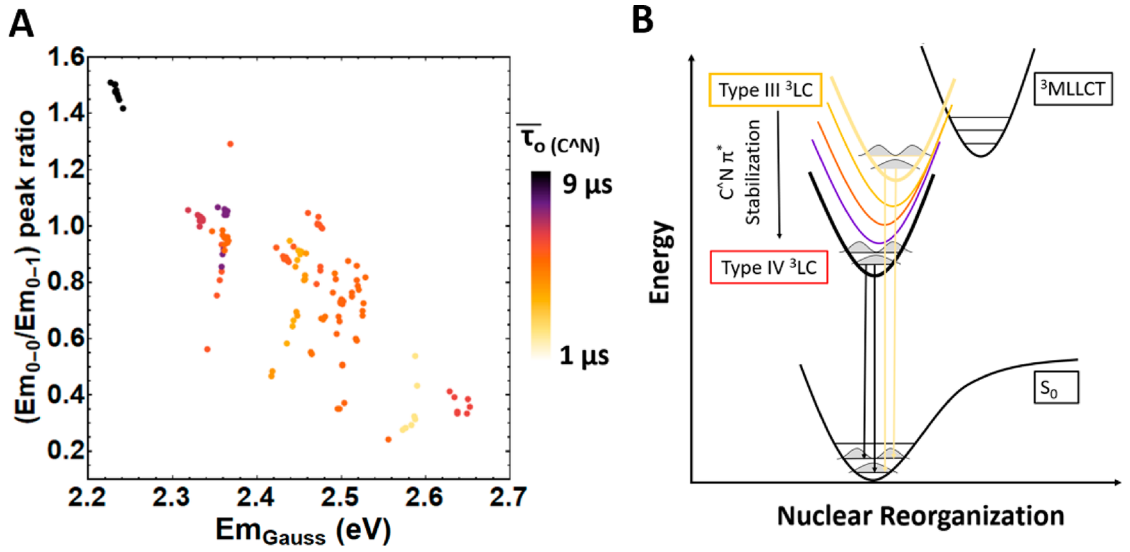

Figure 9. (A) The ratio of vibronic peaks (Em_{0-0}/Em_{0-1}) vs $Em_{Gauss}(Em_{0-0})$ of Ir(III) complexes containing **CN29, CN31, CN33, CN34, CN37, CN38, CN39, CN40, CN42, CN44, CN48, CN67, CN94, CN95** with **NN1, NN2, NN3, NN6, NN8, NN16, NN20, NN26, NN33, NN47**. Selected C^N ligands are most likely to from Type III/IV excited states. The average lifetime of each family of complexes that contain the same cyclometalating ligand ($\overline{\tau}_{o\ (C^N)}$)) with different ancillary ligands corresponds to plot point color. (B) Relative energy level diagram of Type III/IV excited states, depicting the interplay of triplet emission and nuclear reorganization. The lower lying ^{3}LC states in Type IV complexes are much less likely to be perturbed by the ^{3}MLLCT state.

While both 2,2′-bipyridine and 1,10-phenanthroline containing heteroleptic complexes may have similar $k_{nr}(E_{gap})$ dictated by the Energy Gap Law, $k_{nr}(^3MC)$ is much lower for 1,10-phenanthroline. It is important to note that this behavior could in part be rationalized by differences of vibronic coupling modes between T_1 and S_0 in Type I ^{3}MLLCT excited states associated with 2,2′-bipyridine, but it would be inhibited with the more rigid 1,10-phenanthroline; although, all excited state morphologies (Type I−Type IV) exhibit the same trends on the basis of ancillary ligand identity, even if the excited state is predominately or exclusively localized on the C^N ligand (Type III, Type IV). Vibronic deactivation pathways involving the diimine ligand should not control the photophysical properties of ^{3}LC dominated excited states. Population of ^{3}MC states through weakened coordination environment therefore explains the behavior observed across the entire data set most consistently.

A similar trend is observed dependent on substituent group positioning around the chelating nitrogen on the ancillary N^N ligand. Lifetimes of complexes containing ancillary ligand 5,5′-dimethyl-2,2′-bipyridine (**NN3**) compared to **NN2** favor the former across all excited state morphologies (Type I−Type IV) with respect to higher lifetimes (Figure 8B). Further comparisons of complex lifetimes with **NN3** and the N^N ligand 4,4′-di-*tert*-butyl-2,2′-bipyridine (**NN6**) and 4,4′-dimethoxy-2,2′-bipyridine (**NN8**) again show **NN3** yielding higher lifetimes for the same C^N ligand (Figure 8B). A concurrent increase in emission intensity is also observed, essentially mirroring the behavior observed between 2,2′-bipyridine and 1,10-phenanthroline. Modes of nuclear reorganization in the excited state may differ and depend on substituent group positioning, resulting in similar photophysical trends between **NN3** and other 1,10-phenanthroline based N^N ligands.

Lifetimes in ^{3}LC excited states are more challenging to understand and control due to a complex interplay between the Ir *d* orbital contribution to the excited state and nuclear reorganization effects. Although excited state lifetimes of ^{3}LC states are typically longer than ^{3}MLLCT, the large spread of excited state lifetimes (∼1−12 μs) suggests numerous factors contributing to nonradiative decay pathways. ^{3}LC states offer the unique advantages of quantifying differing nuclear geometries between the ground and triplet excited state by comparing the intensities of the two highest energy vibronic transitions ($Em_{0-0}(Em_{Gauss})$ and Em_{0-1}, respectively).[55] The ratio between these two vibronic emission bands (Em_{0-0}/Em_{0-1}) provides an approximation of the nuclear reorganization that occurs upon transitioning from T_1 to S_0, consistent with the Franck−Condon Principle (Figure 9B). Type IV excited states are characterized by a large ratio ($Em_{0-0}/Em_{0-1} \geq 1$) that signifies a similar nuclear position between ground and excited state as Em_{0-0} is more intense. As the peak ratio decreases, transitioning from Type IV to Type III excited states, the difference between T_1 and S_0 nuclear geometries continues to increase. Therefore, nuclear distortion increases along with Em_{Gauss}, which is dictated by the ^{3}LC energy of the cyclometalating ligand. The concurrent decrease in the average lifetime across complexes containing a single cyclometalating ligand ($\overline{\tau}_{o\ (C^N)}$) with numerous ancillary ligands exhibits reverse behavior than that predicted by the Energy Gap Law. It is unlikely that the enhancement of nonradiative decay rates arises from the population of the ^{3}MC state. Instead, it is likely that the larger differences between the singlet ground state and the excited triplet state nuclear configurations allow increased rates of nonradiative decay, implying that the nuclear configuration of the triplet excited state may be similar to an excited vibronic configuration of the ground state. Nuclear reorganization is supported through comparison of the heat of formation between the singlet at the optimized singlet geomtery and the singlet at the optimized triplet geomtery ($\Delta H_{Form}(S-S)$) from DFT calculations; a larger difference indicates a more substantially reorganized triplet configuration relative to the singlet. $\Delta H_{Form}(S-S)$ concurrently increases as

https://dx.doi.org/10.1021/jacs.0c12290
J. Am. Chem. Soc. 2021, 143, 1179−1194

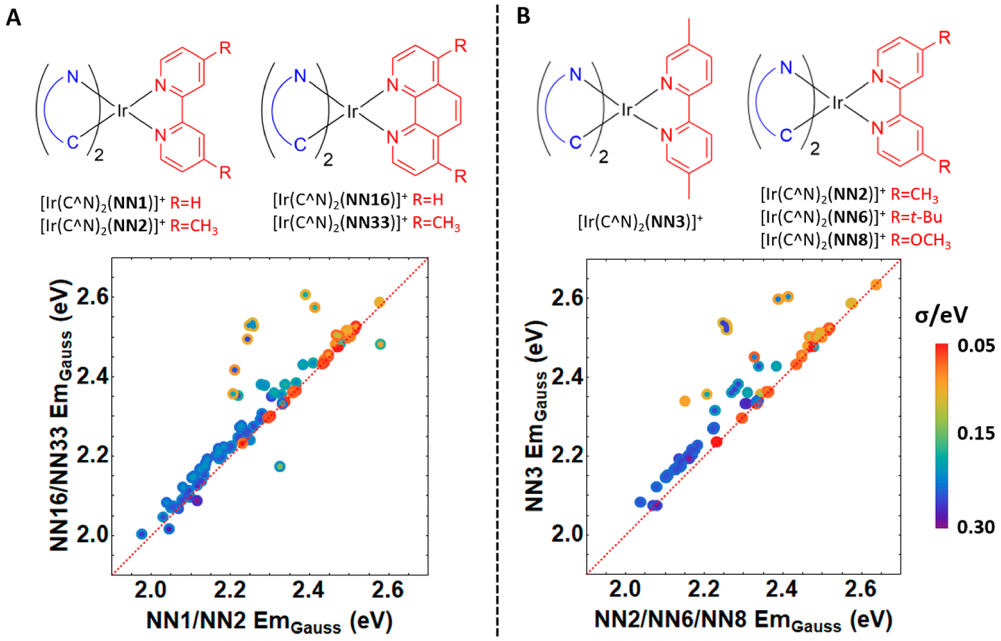

Figure 10. Effect of ligand morphology and substituent position of ancillary ligands on Em_{Gauss}. Representation of the Ir(III) complexes discussed are shown, particularly the ancillary ligands (top). Overlaid comparison plots of Em_{Gauss} for complexes containing all C^N ligands with **NN16** vs **NN1** and the methyl substituted **NN33** vs **NN2** (A) and **NN2**/**NN6**/**NN8** vs **NN3** (B). Equivalent excited states will fall on y = x (red dashed line). Standard deviation of fitted Gaussian function(s) (σ) corresponds to plot point color; for each plot point the outer ring corresponds to spectral fits of **NN16**/**NN33** (A) and of **NN3** (B) complexes, while the inner circle corresponds to those of **NN1**/**NN2** (A) and of **NN2**/**NN6**/**NN8** (B) complexes.

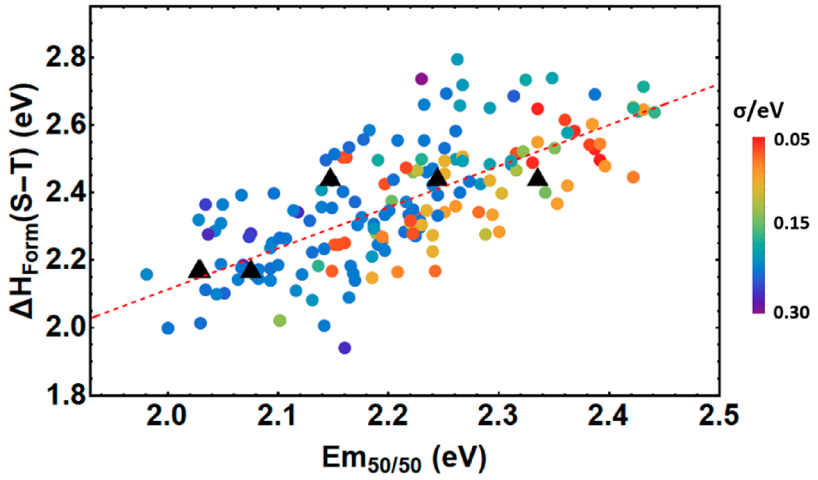

Figure 11. $Em_{50/50}$ correlated with the differences in heat of formations between the singlet and triplet DFT calculations (ΔH_{FORM}(S-T)) at their respective optimized geometries. Plot points are color coded based of σ values used for spectral fitting, showing independence from excited state morphology. Black triangles correspond to complexes previously tested.[43]

the Em_{0-0}/Em_{0-1} peak ratios decrease (Figure S14) for Type III/IV complexes.

Emission Energy Tuning and Prediction. Color tuning in heteroleptic $[Ir(C^N)_2(N^N)]^+$ complexes involves functional group variations on the C^N or N^N ligands to tune the spatially separated HOMO/LUMO orbital energy levels. After Franck−Condon excitation, the ensuing nuclear relaxation to account for the new electronic configuration lowers the energy of the HSOMO. The structural rigidity of 1,10-phenanthroline and its derivatives inhibit relaxation mechanisms involving torsional bond rotation that occur in 2,2′-bipyridine type N^N ligands. Consequently, comparison of Em_{Gauss} of **NN1** and **NN16** (as well as **NN2** and **NN33**) complexes with identical C^N ligands shows that the 1,10-phenanthroline based complexes exhibit a slightly higher luminescence energy in Type I complexes (blue dots, Figure 10A). Despite only slightly more negative reduction potentials of $[Ir(C^N)_2(N^N)]^+$ complexes with 2,2′-bipyridine compared to 1,10-phenanthroline, given the same C^N ligands, it appears that the less rigid **NN1**/**NN2** ligands allow a more substantial structural relaxation following the population of the antibonding π^* orbital in the excited state, lowering the energy of the HSOMO relative to 1,10-phenanthroline counterparts.[41] Complexes containing C^N ligands that induce ^{3}LC dominated excited states greatly decreases the effect of the ancillary ligand and an almost identical luminescence spectrum

https://dx.doi.org/10.1021/jacs.0c12290
J. Am. Chem. Soc. 2021, 143, 1179−1194

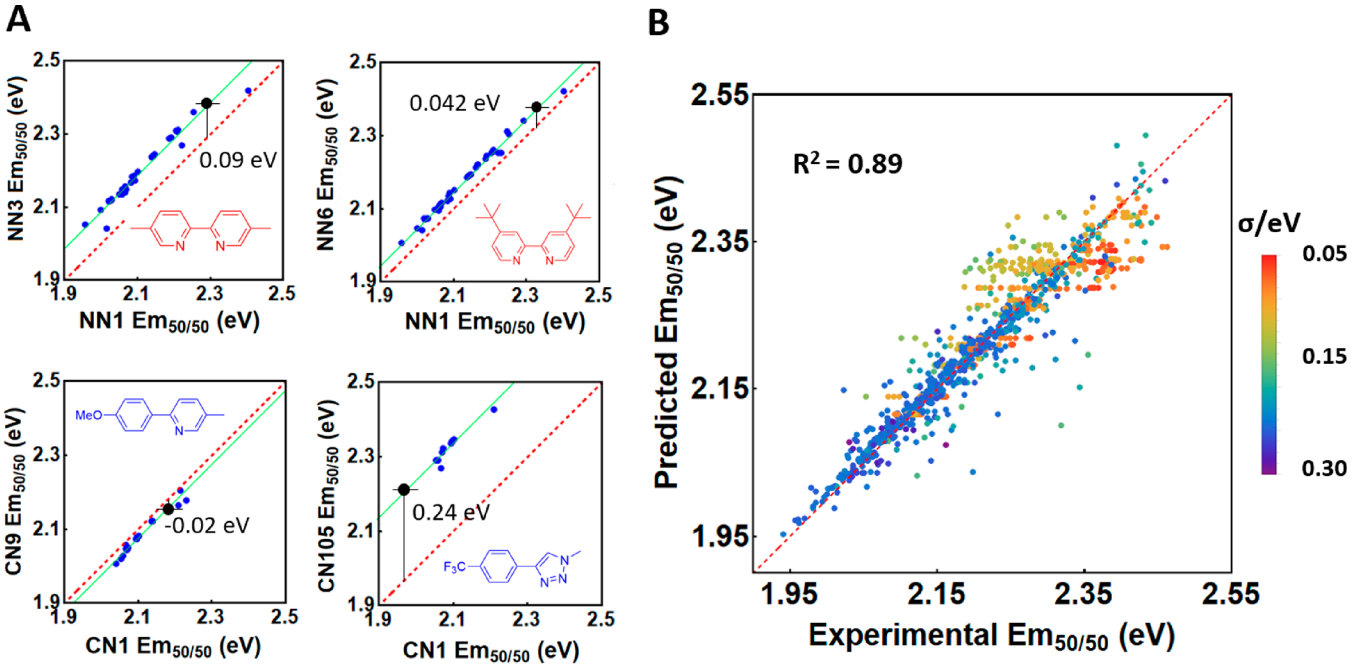

Figure 12. (A) Depiction of methodology for finding E_{offset} for all cyclometalating (top) and ancillary ligands (bottom) relative to **CN1** and **NN1**. The line of best fit for the linear offset was required to have a slope of 1, defining E_{offset} as the y-intercept. Ligand structures are shown. (B) Predicted vs Experimental $Em_{50/50}$ of prepared Ir(III) complexes. Complexes without a measurable excited state lifetime were not included in the model.

is observed. An x,y scatter plot of their Em_{Gauss} values fall on the x = y line, while the ^{3}MLLCT data pairs reveal constant deviation from this line. A few complexes exhibit different excited states between **NN1**/**NN16** and **NN2**/**NN33**, leading to the dramatic displacement from the x = y line (shown by the difference in plot point color). This arises from the capability of 1,10-phenanthroline complexes to populate ^{3}LC states while the 2,2′-bipyridine complexes are ^{3}MLLCT for the same C^N ligand, supporting a higher energy HSOMO due to the rigidity of **NN16**/**NN33**. A similar trend is observed when comparing Em_{Gauss} of complexes containing 5,5′-dimethyl-2,2′-bipyridine (**NN3**) with either 4,4′-dimethyl-2,2′-bipyridine (**NN2**), 4,4′-di-*tert*-butyl-2,2′-bipyridine (**NN6**), or 4,4′-dimethoxy-2,2′-bipyridine (**NN8**): a hypsochromically shifted spectra in the Type I region as well more facile population of the ^{3}LC state located on the C^N ligand (Figure 10B).

Given this expansive set of uniformly measured emission spectra and the general interest of HOMO/LUMO tuning in these compounds, we investigated different models toward predicting emission wavelength. For this process, we found it necessary to use the emission energy where the integral of the spectrum above and below that energy are equal, to account for differences in spectral shape ($Em_{50/50}$) caused by different emission spectral profiles for different triplet excited state configurations. First attempts began with DFT-based modeling, where we replicated previous work by taking the difference in heat of formation between the triplet state at the optimized triplet geometry and the singlet state at the triplet geometry. We found stronger correlations among this much larger data set between the triplet at the optimized triplet geometry and the singlet state at the optimized singlet geometry (ΔH_{FORM}(S-T)) with $Em_{50/50}$ (Figure 11).[43] Interestingly, this linear correlation modeling a much more diverse set of complexes had an R^2 = 0.50; moves to different functionals/basis sets or more complex calculated features will be needed to adequately model emission energy computationally.

The use of a substituent-based model proved to be much more successful. Complexes with Type I excited states (Figure 10, blue dots) are typically linearly offset from the y = x line when comparing Em_{Gauss} with changing C^N ligand identity, while Type IV ^{3}LC states resides on the y = x line (because emission is now exclusively dependent on the C^N ligand, Figure 10). This is commonly observed across all comparison plots of $Em_{50/50}$ (Figure S15–S16). This linear offset in the Type I region can be thought of as an approximate value for the "push-pull" energetic capacity of a particular ligand in reference to another and is therefore a strong predictor for emission color. As such, we calculated these energy shifts of all C^N and N^N ligands compared to **CN1** and **NN1** (Figure 12A), allowing prediction of emission color compared to the archetypal parent compound $[Ir(\mathbf{CN1})_2(\mathbf{NN1})]^+$ using eq 2, where $\mathbf{CN}_i$ and $\mathbf{NN}_j$ represent a unique combination of C^N and N^N ligands forming a specific complex. The four plots in Figure 12A show how the energy offset (E_{offset}), defined in the plot, value is calculated. The right side shows the Predicted vs Experimental plot for $Em_{50/50}$ calculated from eq 2 (Figure 12B)

$$Em_{50/50}(\mathbf{C^N_i}, \mathbf{N^N_j}) = Em_{50/50}(\mathbf{CN1}, \mathbf{NN1}) + C^N_{offset}(\mathbf{i}) + N^N_{offset}(\mathbf{j}) \quad (2)$$

In the case of C^N ligands commonly forming Type III/IV excited states, determined by the standard deviation (σ) used for spectral fitting, the predicted $Em_{50/50}$ is the average across all N^N ligands. Superb predictive power is achieved across the entire library with an R^2 = 0.89. All offset values for each ligand are reported in Figures S15 and S16. Current efforts are directed at correlating this data with quantum chemical calculations.

https://dx.doi.org/10.1021/jacs.0c12290
J. Am. Chem. Soc. 2021, 143, 1179−1194

Analysis of E_{offset} supports the observed hypsochromic shift in emission dependent on N^N ligands as discussed in Figure 10. First off, E_{offset} (**NN16**) = +0.012 eV, meaning $Em_{50/50}$ is about 0.012 eV higher in energy when **NN16** is used with the same C^N compared to **NN1** in ^{3}MLLCT (Type I) excited states. The importance of structural rigidity is again observed when comparing E_{offset} for 4,4′-dimethyl-2,2′-bipyridine (**NN2**) and 4,7-dimethyl-1,10-phenanthroline (**NN33**); E_{offset}(**NN2**) = +0.043 eV whereas E_{offset}(**NN33**) = +0.094 eV. Lastly, the importance of substituent group position is shown when comparing E_{offset} for 5,5′-dimethyl-2,2′-bipyridine (E_{offset}(**NN3**) = +0.094 eV) whereas E_{offset}(**NN2**) = +0.043 eV, E_{offset}(**NN6**) = +0.042 eV, and E_{offset}(**NN8**) = +0.08 eV.

CONCLUSION

Here, we present a framework for assigning the excited state morphology in heteroleptic Ir(III) complexes using only emission spectra and lifetime. Developed from the experimental characterization of an unprecedented combinatorial library, this framework elucidates the following excited state trends:

- The emissive excited state of any given complex is classified as one of four distinct Types defined by the Gaussian fitting parameters of its spectral profile. Type I excited states exhibit broad, featureless emission while Type IV are characterized by resolved vibronic substructure. The nature of the excited state of these two extremes are classified as pure ^{3}MLLCT and ^{3}LC, respectively. Type II excited states are typically non-structured but asymmetrical and Type III exhibit vibronic resolution albeit with a low intensity Em_{0-0} peak. Both Type II/III are therefore characterized as mixed ^{3}MLLCT/^{3}LC character where ^{3}MLLCT dominates the former and ^{3}LC dominates the latter.
- Dependent on the excited state morphology of a complex, lifetime can be rationalized through four dominant factors: (1) the Energy Gap Law, (2) Ir *d* orbital contribution to the excited triplet state, (3) population of ^{3}MC states, and (4) geometrical distortion occurring as a mode of internal conversion after Franck−Condon excitation. Geometrical distortion, specifically torsional bond rotation between the ancillary ligand rings, strongly depends on ligand morphology. This accounts for the very notable differences in photophysical properties between 2,2′-bipyridine and 1,10-phenanthroline ligands and their analogs. Relaxation occurring via torsional bond rotation greatly perturbs the energy of the ^{3}MC state. Consequently, complexes containing rigid ancillary ligands exhibit longer lifetimes, brighter emission, and higher energy Em_{Gauss} peaks. Similar behavior is observed and dependent on substituent group positioning about the coordinating nitrogen atoms.
- Efforts to hypsochromically shift emission spectra toward higher emission energy will be limited to two factors in solution: (1) Type I, ^{3}MLLCT emission above 2.35 eV suffers from population of the ^{3}MC state, resulting in poor quantum yields and (2) significant reorganization in Type III/IV excited state renders the Em_{0-0} transition weak compared to the lower energy Em_{0-1}/Em_{0-2} peaks. Introduction of electron withdrawing groups to increase the HOMO−LUMO gap result in significantly reorganized ^{3}LC states relative to S_0, resulting in a bathochromic Em_{max} compared to Em_{Gauss}/Em_{0-0}.
- A predictive model has been developed which assigns $Em_{50/50}$ to all emissive complexes. This model quantifies the amount of "push-pull" a particular C^N/N^N ligand can afford relative to 2-phenylpyrdine and 2,2′-bipyridine. The predictive success of this model (R^2 = 0.89) is ultimately attributed to the inherent electron richness and vibronic relaxation dynamics characteristic of each ligand.

This framework will enable the rational design of new transition metal phosphors that boast spectral color and lifetime both tailored to the requirements of the end applications. We are currently investigating the implications of these findings on the rate of photoinitiated electron transfer.

EXPERIMENTAL SECTION

Reagents and solvents were purchased from various commercial sources and used without further purification. Nuclear magnetic resonance (NMR) spectra were obtained using a Bruker Avance 500 or 300 MHz spectrometer; ^{1}H spectra were referenced to residual solvent peaks. Cyclometalating ligands were synthesized using adapted procedures from literature and characterized with ^{1}H NMR spectrometry.[43,56−59]

High-Throughput Synthesis of $[Ir(C^N)_2(N^N)]^+$ Cl^- Complexes. Reactions were performed in parallel using an 8*12 plate of 1 mL glass vials tightly sealed with a silicon film coated with Teflon. Aliquots of an iridium dimer solution in dimethyl sulfoxide (0.5 mM, 250 μL) and ancillary ligand in dimethyl sulfoxide (1.0 mM, 250 μL) were combined in each vial and heated at 150 °C for 16 h.

Photophysical Measurements. The prepared iridium(III) complexes were irradiated with a pulsed 365 nm LED, powered by a 40 ns square pulse from a Siglent SDG1052 function generator. Emission was detected with a Hamamatsu H7732−11 photomultiplier tube connected to a Tektronix TDS3032B digital oscilloscope interfaced to a Raspberry Pi 3 Model B+ computer. Scattered light from the excitation source was removed from acquired spectra using a plexiglass filter (365 nm long pass). Emission spectra were measured concurrently using a StellarNet BLACK-Comet concave grating spectrometer and collected without spectral correction of spectrometer sensitivity.

Spectral Deconvolution. Raw emission spectra were imported into Mathematica and successively fit with 1−4 Gaussian functions. The standard deviation (σ) and Gaussian peak spacing were kept constant for fits that required more than one function. No restrictions were placed on the relative amplitude or width of the fitted functions, and the strength of the fit (R^2) was determined via the least-squares method. A higher order fit was used when there existed a significant difference in the strength of fits between a single function and four−five Gaussians ($\Delta R^2 \sim 0.005$). A two-function fit was used if the higher order fit did not significantly improve the calculated R^2. Spectra inadequately fit with this general method were corrected through restrictions of the standard deviation used for fitting.

Computational Modeling. Electronic structure was modeled with singlet and triplet-based Density Functional Theory (DFT) through geometry optimization at the B3LYP level of theory using the LANL2DZ basis set on Gaussian 09.

ASSOCIATED CONTENT

Supporting Information

The Supporting Information is available free of charge at https://pubs.acs.org/doi/10.1021/jacs.0c12290.

Raw spectroscopic data, and extracted features from Gaussian function fitting (PDF)

https://dx.doi.org/10.1021/jacs.0c12290
J. Am. Chem. Soc. 2021, 143, 1179−1194

Raw spectroscopic data, and extracted features from Gaussian function fitting (XLSX)

Raw spectroscopic data, and extracted features from Gaussian function fitting (XLSX)

AUTHOR INFORMATION

Corresponding Author

Stefan Bernhard − *Department of Chemistry, Carnegie Mellon University, Pittsburgh, Pennsylvania 15213, United States;* orcid.org/0000-0002-8033-1453; Email: bern@cmu.edu

Authors

Stephen DiLuzio − *Department of Chemistry, Carnegie Mellon University, Pittsburgh, Pennsylvania 15213, United States*

Velabo Mdluli − *Department of Chemistry, Carnegie Mellon University, Pittsburgh, Pennsylvania 15213, United States*

Timothy U. Connell − *Department of Chemistry, Carnegie Mellon University, Pittsburgh, Pennsylvania 15213, United States;* orcid.org/0000-0002-6142-3854

Jacqueline Lewis − *Department of Chemistry, Carnegie Mellon University, Pittsburgh, Pennsylvania 15213, United States*

Victoria VanBenschoten − *Department of Chemistry, Carnegie Mellon University, Pittsburgh, Pennsylvania 15213, United States*

Complete contact information is available at: https://pubs.acs.org/10.1021/jacs.0c12290

Notes

The authors declare no competing financial interest.

ACKNOWLEDGMENTS

We are grateful for the financial support of the US NSF (CHE-1764353) and Carnegie Mellon's Manufacturing Futures Initiative that is funded by the Richard King Mellon Foundation. T.U.C. was supported by a Fulbright Future Scholarship. NMR instrumentation at Carnegie Mellon University was partially supported by the NSF (CHE-1039870 and CHE-1726525).

REFERENCES

(1) Gao, R.; Ho, D. G.; Hernandez, B.; Selke, M.; Murphy, D.; Djurovich, P. I.; Thompson, M. E. Bis-cyclometalated Ir(III) Complexes as Efficient Singlet Oxygen Sensitizers. *J. Am. Chem. Soc.* **2002**, *124*, 14828−14829.

(2) Goldsmith, J. I.; Hudson, W. R.; Lowry, M. S.; Anderson, T. H.; Bernhard, S. Discovery and High-Throughput Screening of Heteroleptic Iridium Complexes for Photoinduced Hydrogen Production. *J. Am. Chem. Soc.* **2005**, *127*, 7502−7510.

(3) Slinker, J. D.; Gorodetsky, A. A.; Lowry, M. S.; Wang, J.; Parker, S.; Rohl, R.; Bernhard, S.; Malliaras, G. G. Efficient Yellow Electroluminescence from a Single Layer of a cyclometalated iridium complex. *J. Am. Chem. Soc.* **2004**, *126*, 2763−2767.

(4) Cline, E. D.; Adamson, S. E.; Bernhard, S. Homogeneous Catalytic System for Photoinduced Hydrogen Production utilizing Iridium and Rhodium catalyst. *Inorg. Chem.* **2008**, *47* (22), 10378−10388.

(5) Tsuboyama, A.; Iwawaki, H.; Furugori, M.; Mukaide, T.; Kamatani, J.; Igawa, S.; Moriyama, T.; Miura, S.; Takiguchi, T.; Okada, S.; Hoshino, M.; Ueno, K. Homoleptic Cyclometalated Iridium Complexes with Highly efficient red photosphorescence and application to organic LED. *J. Am. Chem. Soc.* **2003**, *125*, 12971−12979.

(6) Zhang, P.; Guo, J.; Wang, Y.; Pang, W. Incorporation of luminescent tris(bipyridine)ruthenium(II) complex in mesoporous silica spheres and their spectroscopic and oxygen sensing properties. *Mater. Lett.* **2002**, *53*, 400−405.

(7) Laskar, I. R.; Chen, T.-M. Tuning of Wavelengths: Synthesis and Photophysical Studies of Iridium Complexes and Their Applications in Organic Light Emitting Devices. *Chem. Mater.* **2004**, *16*, 111−117.

(8) Babak, M. V.; Le Faouder, P.; Trivelli, X.; Venkatesan, G.; Bezzubov, S. I.; Kajjout, M.; Gushchin, A. L.; Hanif, M.; Poizat, O.; Vezin, H.; Rolando, C. Heteroleptic Ruthenium(II) Complexes with Bathophenanthroline and Bathophenanthroline Disulfonate Disodium Salt as Fluorescent Dyes for In-Gel Protein Staining. *Inorg. Chem.* **2020**, *59* (7), 4527−4535.

(9) Connell, T. U.; Fraser, C. L.; Czyz, M. L.; Smith, Z. M.; Hayne, D. J.; Doeven, E. H.; Agugiaro, J.; Wilson, D. J. D.; Adcock, J. L.; Scully, A. D.; Gomez, D. E.; Barnett, N. W.; Polyzos, A.; Francis, P. S. The Tandem Photoredox Catalysis Mechanism of $[Ir(ppy)_2(dtb\text{-}bpy)](+)$ Enabling Access to Energy Demanding Organic Substrates. *J. Am. Chem. Soc.* **2019**, *141* (44), 17646−17658.

(10) Mdluli, V.; Diluzio, S.; Lewis, J.; Kowalewski, J. F.; Connell, T. U.; Yaron, D.; Kowalewski, T.; Bernhard, S. High-throughput Synthesis and Screening of Iridium(III) Photocatalysts for the Fast and Chemoselective Dehalogenation of Aryl Bromides. *ACS Catal.* **2020**, *10* (13), 6977−6987.

(11) Curtin, P. N.; Tinker, L. L.; Burgess, C. M.; Cline, E. D.; Bernhard, S. Structure-activity correlations among iridium(III) photosensitizers in a robust water-reducing system. *Inorg. Chem.* **2009**, *48* (22), 10498−10506.

(12) Ding, W.; Lu, L. Q.; Liu, J.; Liu, D.; Song, H. T.; Xiao, W. J. Visible Light Photocatalytic Radical-Radical Cross-Coupling Reactions of Amines and Carbonyls: A Route to 1,2-Amino Alcohols. *J. Org. Chem.* **2016**, *81* (16), 7237−7243.

(13) Gartner, F.; Cozzula, D.; Losse, S.; Boddien, A.; Anilkumar, G.; Junge, H.; Schulz, T.; Marquet, N.; Spannenberg, A.; Gladiali, S.; Beller, M. Synthesis, characterisation and application of iridium(III) photosensitisers for catalytic water reduction. *Chem. - Eur. J.* **2011**, *17* (25), 6998−7006.

(14) Huan, F.; Chen, Q. Y.; Guo, Y. Visible Light-Induced Photoredox Construction of Trifluoromethylated Quaternary Carbon Centers from Trifluoromethylated Tertiary Bromides. *J. Org. Chem.* **2016**, *81* (16), 7051−7063.

(15) Huang, H.; Banerjee, S.; Sadler, P. J. Recent Advances in the Design of Targeted Iridium(III) Photosensitizers for Photodynamic Therapy. *ChemBioChem* **2018**, *19* (15), 1574−1589.

(16) Jiang, X.; Peng, J.; Wang, J.; Guo, X.; Zhao, D.; Ma, Y. Iridium-Based High-Sensitivity Oxygen Sensors and Photosensitizers with Ultralong Triplet Lifetimes. *ACS Appl. Mater. Interfaces* **2016**, *8* (6), 3591−3600.

(17) Khan, S. N.; Zaman, M. K.; Li, R.; Sun, Z. A General Method for Photocatalytic Decarboxylative Hydroxylation of Carboxylic Acids. *J. Org. Chem.* **2020**, *85* (7), 5019−5026.

(18) Dedeian, K.; Shi, J.; Shepherd, N.; Forsythe, E.; Morton, D. C. Photophysical and Electrochemical Properties of Heteroleptic Tris-Cyclometalated Iridium(III) Complexes. *Inorg. Chem.* **2005**, *44* (13), 4445−4447.

(19) Lo, K. K. Luminescent Rhenium(I) and Iridium(III) Polypyridine Complexes as Biological Probes, Imaging Reagents, and Photocytotoxic Agents. *Acc. Chem. Res.* **2015**, *48* (12), 2985−2995.

(20) Shaw, M. H.; Twilton, J.; MacMillan, D. W. Photoredox Catalysis in Organic Chemistry. *J. Org. Chem.* **2016**, *81* (16), 6898−6926.

(21) Tan, G.; Chen, S.; Sun, N.; Li, Y.; Fortin, D.; Wong, W.-Y.; Kwok, H.-S.; Ma, D.; Wu, H.; Wang, L.; Harvey, P. D. Highly efficient iridium(iii) phosphors with phenoxy-substituted ligands and their high-performance OLEDs. *J. Mater. Chem. C* **2013**, *1* (4), 808−821.

(22) Tong, B.; Ku, H.-Y.; Chen, I. J.; Chi, Y.; Kao, H.-C.; Yeh, C.-C.; Chang, C.-H.; Liu, S.-H.; Lee, G.-H.; Chou, P.-T. Heteroleptic Ir(III)

phosphors with bis-tridentate chelating architecture for high efficiency OLEDs. *J. Mater. Chem. C* **2015**, *3* (14), 3460−3471.
(23) Karges, J.; Heinemann, F.; Jakubaszek, M.; Maschietto, F.; Subecz, C.; Dotou, M.; Vinck, R.; Blacque, O.; Tharaud, M.; Goud, B.; Vinuelas Zahi Nos, E.; Spingler, B.; Ciofini, I.; Gasser, G. Rationally Designed Long-Wavelength Absorbing Ru(II) Polypyridyl Complexes as Photosensitizers for Photodynamic Therapy. *J. Am. Chem. Soc.* **2020**, *142* (14), 6578−6587.
(24) Tong, B.; Ku, H.-Y.; Chen, I. J.; Chi, Y.; Kao, H.-C.; Yeh, C.-C.; Chang, C.-H.; Liu, S.-H.; Lee, G.-H.; Chou, P.-T. Heteroleptic Ir(III) phosphors with bis-tridentate chelating architecture for high efficiency OLEDs. *J. Mater. Chem. C* **2015**, *3* (14), 3460−3471.
(25) Wang, Z.; He, L.; Duan, L.; Yan, J.; Tang, R.; Pan, C.; Song, X. Blue-green emitting cationic iridium complexes with 1,3,4-oxadiazole cyclometallating ligands: synthesis, photophysical and electrochemical properties, theoretical investigation and electroluminescent devices. *Dalton Trans.* **2015**, *44* (36), 15914−15923.
(26) Ross, D. A.; Scattergood, P. A.; Babaei, A.; Pertegas, A.; Bolink, H. J.; Elliott, P. I. Luminescent osmium(ii) bi-1,2,3-triazol-4-yl complexes: photophysical characterisation and application in light-emitting electrochemical cells. *Dalton Trans.* **2016**, *45* (18), 7748−7757.
(27) Connell, T. U.; Donnelly, P. S. Labelling proteins and peptides with phosphorescent d6 transition metal complexes. *Coord. Chem. Rev.* **2018**, *375*, 267−284.
(28) Deaton, J. C.; Castellano, F. N. *Archetypal Iridium(III) Compounds for Optoelectronic Applications Photophysical Properties and Synthetic Methods*. First ed. ed., John Wiley & Sons Lt: NJ, 2017.
(29) Younker, J. M.; Dobbs, K. D. Correlating Experimental Photophysical Properties of Iridium(III) Complexes to Spin-Orbit Coupled TDDFT Predictions. *J. Phys. Chem. C* **2013**, *117* (48), 25714−25723.
(30) Pomarico, E.; Silatani, M.; Messina, F.; Braem, O.; Cannizzo, A.; Barranoff, E.; Klein, J. H.; Lambert, C.; Chergui, M. Dual Luminescence, Interligand Decay, and Nonradiative Electronic Relaxation of Cyclometalated Iridium Complexes in Solution. *J. Phys. Chem. C* **2016**, *120* (30), 16459−16469.
(31) Kim, J.-H.; Kim, S.-Y.; Cho, Y.-J.; Son, H.-J.; Cho, D. W.; Kang, S. O. A Detailed Evaluation for the Nonradiative Processes in Highly Phosphorescent Iridium(III) Complexes. *J. Phys. Chem. C* **2018**, *122* (7), 4029−4036.
(32) Kim, J. H.; Kim, S. Y.; Jang, S.; Yi, S.; Cho, D. W.; Son, H. J.; Kang, S. O. Blue Phosphorescence with High Quantum Efficiency Engaging the Trifluoromethylsulfonyl Group to Iridium Phenylpyridine Complexes. *Inorg. Chem.* **2019**, *58* (23), 16112−16125.
(33) Wu, S.-H.; Ling, J.-W.; Lai, S.-H.; Huang, M.-J.; Cheng, C. H.; Chen, I.-C. Dynamics of the Excited States of $[Ir(ppy)_2\ bpy]^+$ with Triple Phosphorescence. *J. Phys. Chem. A* **2010**, *114* (38), 10339−10344.
(34) You, Y.; Park, S. Y. Phosphorescent iridium(III) complexes: toward high phosphorescence quantum efficiency through ligand control. *Dalton Trans.* **2009**, *8*, 1267−1282.
(35) Colombo, M. G.; Hauser, A.; Giidel, H. U. Evidence for Strong Mixing between the LC and MLCT Excited States in Bis(2-phenylpyridinato-C^2,N')(2,2′-bipyridine)iridium(III). *Inorg. Chem.* **1993**, *32* (14), 3088−3092.
(36) Yang, C.-H.; Li, S.-W.; Chi, Y. Heteroleptic Cyclometalated Iridium(III) Complexes Displaying Blue Phosphorescence in Solution and Solid State at Room Temperature. *Inorg. Chem.* **2005**, *44* (22), 7770−7780.
(37) Tamayo, A. B.; Garon, S.; Sajoto, T.; Djurovich, P. I.; Tsyba, I. M.; Bau, R.; Thompson, M. E. Cationic Bis-cyclometalated Iridium-(III) Diimine Complexes and Their Use in Efficient Blue, Green, and Red Electroluminescent Devices. *Inorg. Chem.* **2005**, *44* (24), 8723−8732.
(38) Beyer, B.; Ulbricht, C.; Escudero, D.; Friebe, C.; Winter, A.; González, L.; Schubert, U. S. Phenyl-1H-[1,2,3]triazoles as New Cyclometalating Ligands for Iridium(III) Complexes. *Organometallics* **2009**, *28* (18), 5478−5488.
(39) Ladouceur, S.; Fortin, D.; Zysman-Colman, E. Enhanced luminescent iridium(III) complexes bearing aryltriazole cyclometallated ligands. *Inorg. Chem.* **2011**, *50* (22), 11514−11526.
(40) Zanoni, K. P.; Kariyazaki, B. K.; Ito, A.; Brennaman, M. K.; Meyer, T. J.; Murakami Iha, N. Y. Blue-green iridium(III) emitter and comprehensive photophysical elucidation of heteroleptic cyclometalated iridium(III) complexes. *Inorg. Chem.* **2014**, *53* (8), 4089−4099.
(41) Monti, F.; Baschieri, A.; Gualandi, I.; Serrano-Perez, J. J.; Junquera-Hernandez, J. M.; Tonelli, D.; Mazzanti, A.; Muzzioli, S.; Stagni, S.; Roldan-Carmona, C.; Pertegas, A.; Bolink, H. J.; Orti, E.; Sambri, L.; Armaroli, N. Iridium(III) complexes with phenyltetrazoles as cyclometalating ligands. *Inorg. Chem.* **2014**, *53* (14), 7709−7721.
(42) Scattergood, P. A.; Ranieri, A. M.; Charalambou, L.; Comia, A.; Ross, D. A. W.; Rice, C. R.; Hardman, S. J. O.; Heully, J. L.; Dixon, I. M.; Massi, M.; Alary, F.; Elliott, P. I. P. Unravelling the Mechanism of Excited-State Interligand Energy Transfer and the Engineering of Dual Emission in $[Ir(C^N)_2(N^N)]^+$ Complexes. *Inorg. Chem.* **2020**, *59* (3), 1785−1803.
(43) Lowry, M. S.; Hudson, W. R.; Pascal, R. A.; Bernhard, S. Accelerated Luminophore Discovery through Combinatorial Synthesis. *J. Am. Chem. Soc.* **2004**, *126*, 14129−14135.
(44) Lowry, M. S.; Bernhard, S. Synthetically tailored excited states: phosphorescent, cyclometalated iridium(III) complexes and their applications. *Chem. - Eur. J.* **2006**, *12* (31), 7970−7977.
(45) Hasan, K.; Bansal, A. K.; Samuel, I. D. W.; Roldán-Carmona, C.; Bolink, H. J.; Zysman-Colman, E. Tuning the Emission of Cationic Iridium (III) Complexes Towards the Red Through Methoxy Substitution of the Cyclometalating Ligand. *Sci. Rep.* **2015**, *5*, 1.
(46) Hay, P. J. Theoretical Studies of the Ground and Excited Electronic States in Cyclometalated Phenylpyridine Ir(III) Complexes Using Density Functional Theory. *J. Phys. Chem. A* **2002**, *106*, 1634−1641.
(47) Sajoto, T.; Djurovich, P.; Tamayo, A.; Oxgaard, J.; Goddard, W.; Thompson, M. Temperature Dependence of Blue Phosphorescent Cyclometalated Ir(III) Complexes. *J. Am. Chem. Soc.* **2009**, *131*, 9813−9822.
(48) Escudero, D. Quantitative prediction of photoluminescence quantum yields of phosphors from first principles. *Chem. Sci.* **2016**, *7* (2), 1262−1267.
(49) Jacquemin, D.; Escudero, D. The short device lifetimes of blue PhOLEDs: insights into the photostability of blue Ir(iii) complexes. *Chem. Sci.* **2017**, *8* (11), 7844−7850.
(50) Costa, R. D.; Ortí, E.; Tordera, D.; Pertegás, A.; Bolink, H. J.; Graber, S.; Housecroft, C. E.; Sachno, L.; Neuburger, M.; Constable, E. C. Stable and Efficient Solid-State Light-Emitting Electrochemical Cells Based on a Series of Hydrophobic Iridium Complexes. *Adv. Energy Mater.* **2011**, *1* (2), 282−290.
(51) Wang, X.; Wang, S.; Pan, F.; He, L.; Duan, L. Cationic Iridium Complexes with 5-Phenyl-1H-1,2,4-triazole Type Cyclometalating Ligands: Toward Blue-Shifted Emission. *Inorg. Chem.* **2019**, *58* (18), 12132−12145.
(52) King, K. A.; Watts, R. J. Dual Emission from an Ortho-Metalated Ir(III) Complex. *J. Am. Chem. Soc.* **1987**, *109*, 1589−1590.
(53) Abrahamsson, M.; Lundqvist, M. J.; Wolpher, H.; Johansson, O.; Eriksson, L.; Bergquist, J.; Rasmussen, T.; Becker, H.-C.; Hammarström, L.; Norrby, P.-O.; Åkermark, B.; Persson, P. Steric Influence on the Excited-State Lifetimes of Ruthenium Complexes with Bipyridyl-Alkanylene-Pyridyl Ligand. *Inorg. Chem.* **2008**, *47* (9), 3540−3548.
(54) Kreitner, C.; Erdmann, E.; Seidel, W. W.; Heinze, K. Understanding the Excited State Behavior of Cyclometalated Bis(tridentate)ruthenium(II) Complexes: A Combined Experimental and Theoretical Study. *Inorg. Chem.* **2015**, *54* (23), 11088−11104.
(55) Cho, Y. J.; Kim, S. Y.; Son, H. J.; Cho, D. W.; Kang, S. O. The effect of interligand energy transfer on the emission spectra of

https://dx.doi.org/10.1021/jacs.0c12290
J. Am. Chem. Soc. 2021, 143, 1179−1194

heteroleptic Ir complexes. *Phys. Chem. Chem. Phys.* **2017**, *19* (13), 8778−8786.
(56) Antilla, J. C.; Baskin, J. M.; Barder, T. E.; Buchwald, S. T. Copper Diamine Catalyzed N-Arylation of Pyrroles, Pyrazoles, Inazoles Imidazoles and Triazoles. *J. Org. Chem.* **2004**, *69*, 5578−5587.
(57) Sedaghat, N.; Naimi-Jamal, M. R.; Mokhtari, J. Solvent- and catalyst-free synthesis of 2-aryl(heteroaryl)-substituted benzothiazoles. *Curr. Chem. Lett.* **2014**, *3* (2), 57−62.
(58) Connell, T. U.; White, J. M.; Smith, T. A.; Donnelly, P. S. Luminescent Iridium(III) Cyclometalated Complexes with 1,2,3-Triazole "Click" Ligands. *Inorg. Chem.* **2016**, *55* (6), 2776−2790.
(59) Ghodbane, A.; D'Alterio, S.; Saffon, N.; McClenaghan, N. D.; Scarpantonio, L.; Jolinat, P.; Fery-Forgues, S. Facile access to highly fluorescent nanofibers and microcrystals via reprecipitation of 2-phenyl-benzoxazole derivatives. *Langmuir* **2012**, *28* (1), 855−863.

https://dx.doi.org/10.1021/jacs.0c12290
J. Am. Chem. Soc. 2021, 143, 1179−1194